Diapycnal motion, diffusion, and stretching of tracers in the ocean

Henri F. Drake,[a,b] Xiaozhou Ruan,[c] Raffaele Ferrari,[c]

[a] *Princeton University / Geophysical Fluid Dynamics Laboratory*
[b] *Previously, MIT–WHOI Joint Program in Oceanography/Applied Ocean Science & Engineering, Cambridge and Woods Hole, Massachusetts.*
[c] *Massachusetts Institute of Technology, Department of Earth, Atmospheric, and Planetary Sciences*

Corresponding author: Henri F. Drake, henrifdrake@gmail.com

ABSTRACT: Small-scale mixing drives the diabatic upwelling that closes the abyssal ocean overturning circulation. Measurements of in-situ turbulence reveal that mixing is bottom-enhanced over rough topography, implying downwelling in the interior and stronger upwelling in a sloping bottom boundary layer. However, in-situ mixing estimates are indirect and the inferred vertical velocities have not yet been confirmed. Purposeful releases of inert tracers, and their subsequent spreading, have been used to independently infer turbulent diffusivities; however, these Tracer Release Experiments (TREs) provide estimates in excess of in-situ ones. In an attempt to reconcile these differences, Ruan and Ferrari (2021) derived exact buoyancy moment diagnostics, which we here apply to quasi-realistic simulations. We show in a numerical simulation that tracer-averaged diapycnal motion is directly driven by the tracer-averaged buoyancy velocity, a convolution of the asymmetric upwelling/downwelling dipole. Diapycnal spreading, however, involves both the expected contribution from the tracer-averaged in-situ diffusion and an additional non-linear diapycnal stretching term. These diapycnal stretching effects, caused by correlations between buoyancy and the buoyancy velocity, can either enhance or reduce tracer spreading. Diapycnal stretching in the stratified interior is compensated by diapycnal contraction near the bottom; for simulations of the Brazil Basin Tracer Release Experiment these nearly cancel by coincidence. By contrast, a numerical tracer released near the bottom experiences leading-order stretching that varies in time. These results suggest mixing estimates from TREs are not unambiguous, especially near topography, and that more attention should be paid towards the evolution of tracers' first moments.

1. Introduction

The lower limb of the ocean's meridional overturning circulation traces the diabatic life cycle of abyssal bottom waters (Talley 2013), which store vast quantities of climatically-active tracers like heat and carbon. Bottom waters are formed at the surface of the Southern Ocean by atmospheric cooling and brine rejection and are consumed in the deep ocean by buoyancy-flux convergence due to small-scale mixing and geothermal heating (Abernathey et al. 2016; de Lavergne et al. 2016b). Since mixing processes are too small to be resolved by large-scale ocean models, the rate at which tracers are mixed across density surfaces– the diapycnal diffusivity– enters as a key free parameter in ocean and climate models (Bryan and Lewis 1979; Simmons et al. 2004; de Lavergne et al. 2020). While early models of the abyssal circulation assume this mixing to be spatially uniform (Munk 1966; Stommel and Arons 1959), subsequent in-situ observations reveal a complex geography of mixing processes (e.g. Polzin et al. 1997; Waterhouse et al. 2014). A robust pattern that emerges from these in-situ mixing observations is the bottom-enhancement of mixing over rough topography, consistent with theoretical arguments that this mixing is predominantly caused by breaking internal waves radiating from flow over topography (Munk and Wunsch 1998; Polzin 2009; Nikurashin and Ferrari 2009; Nikurashin and Legg 2011; MacKinnon et al. 2017; Whalen et al. 2020).

The observed bottom-enhancement of deep mixing demands a revision of classic abyssal circulation theory: in the stratified interior, bottom-enhanced mixing above rough topography results in a layer of buoyancy flux divergence—the downwelling Stratified Mixing Layer (SML)—and a thin layer of even larger buoyancy flux convergence at the insulating[1] seafloor—the upwelling Bottom Boundary Layer (BBL). These ideas were first introduced as the regional scale in the Brazil Basin (Polzin et al. 1997; Ledwell et al. 2000; St. Laurent et al. 2001; Huang and Jin 2002) and then generalized to the global context by (Ferrari et al. 2016; McDougall and Ferrari 2017; Callies and Ferrari 2018). The global diabatic overturning circulation is the small residual of substantial downwelling in the SML and even larger upwelling in the BBL (Ferrari et al. 2016; Drake et al. 2020). While the existence of these upwelling/downwelling flows is virtually guaranteed by the combination of a bottom-enhanced turbulent buoyancy flux and an insulating boundary condition along a sloping seafloor, their structure, magnitudes, and underlying dynamics remain poorly

[1]Geothermal heat flux into the BBL acts to amplify upwelling, but is thought to be secondary to mixing globally (de Lavergne et al. 2016a) and is negligible in the Brazil Basin subregion considered here (Thurnherr et al. 2020).

understood (Callies 2018; Drake et al. 2020; Polzin and McDougall 2022). Since diapycnal (or vertical) velocities and fluxes are challenging to measure directly due to the ocean's small aspect ratio, indirect methods must be used to infer the flow, such as volume or buoyancy budgets (e.g. St. Laurent et al. 2001; Lele et al. 2021). Watermass transformation analysis is a commonly-used framework which combines volume and buoyancy budgets to express diapycnal transport across a buoyancy surface in terms of the average turbulent buoyancy flux along the surface, which can be inferred from indirect observations (Walin 1982; Marshall et al. 1999; de Lavergne et al. 2016b; Ferrari et al. 2016; Spingys et al. 2021).

There are several observational methods for estimating in-situ turbulent buoyancy fluxes and their corresponding diffusivities (listed roughly in order of decreasing accuracy and generality; Gregg et al. 2018): 1) velocity variance microstructure based on an approximate turbulent kinetic energy budget (Osborn 1980), 2) temperature variance microstructure based on an approximate temperature variance budget (Osborn and Cox 1972), 3) scaling analysis based on the Thorpe scale of density overturns (Thorpe and Deacon 1977; Dillon 1982), and 4) shear/strain variance finestructure based on idealized spectral models of internal wave dynamics (e.g. Garrett and Munk 1972, 1975; Henyey et al. 1986; Gregg 1989; Polzin et al. 1995; Gregg et al. 2003; Kunze et al. 2006). All of these methods are indirect and require some degree of approximation to convert the measured quantity into a diffusivity. Furthermore, they provide only localized snapshots of spatially and temporally intermittent mixing events and thus may provide biased estimates of the mean diffusivity (Whalen 2021), which is often the goal of parameterization.

Tracer (or Dye[2]) Release Experiments (TREs; Watson et al. 1988) are considered by many to provide the gold standard of mixing rate estimates. In TREs, an assumed inert chemical tracer is deliberately injected into the ocean and its distribution is surveyed by ship-board rosette sampling over timescales of months to years. The evolution of the tracer is then inverted (using approximate advection-diffusion models) to yield estimates of the mean diffusivity and velocity, which can be compared to independent in-situ turbulence measurements. Localized TREs are experimental analogues of mathematicians' Green's function approach and are easier to interpret than thermodynamic or biogeochemical tracers with less well known initial or boundary conditions and more complicated dynamics and mixing histories (e.g. Hogg et al. 1982; Lumpkin and Speer

[2]Fluorescent dye can be used for timescales of hours to days and can be sampled as much higher resolution with in-situ fluorometers (e.g. Ledwell et al. 2004), or—for near-surface releases—remote sensing instruments (Sundermeyer et al. 2007).

2007; Trossman et al. 2020). However, the results of the TRE inversion process still depend upon the assumptions made to infer the diffusivity from simple advection-diffusion forward models.

Watson et al. (1988) pitch TREs in the ocean as an "unambiguous measure of the diapycnal mixing rate" since tracers average over the spatial and temporal variability that challenges the interpretation of in-situ mixing estimates; for example, Watson et al. (1988) hypothesize that the sparse sampling of log-normally distributed (or worse, log-skew-normal) mixing events by in-situ microstructure measurements risks under-estimating mean mixing rates (see also Baker and Gibson 1987; Cael and Mashayek 2021). Superficially, observations from two deep-ocean TREs seem to corroborate this hypothesis: tracer-based estimates of mixing rates are ubiquitously 1.5–10 times larger than co-located in-situ microstructure measurements (Ledwell et al. 2000; Watson et al. 2013; Mashayek et al. 2017). While there are ad-hoc and site-specific explanations for each of these discrepancies, there is no consensus on how best to compare tracer-based and microstructure-based estimates (Gregg et al. 2018), nor what to make of the fact that tracer-based estimates seem to always exceed microstructure-based estimates.

Recent advances in the numerical modelling and theory of TREs provide some guidance for interpreting tracer-based estimates of mixing and comparing them to microstructure-based estimates. For example, Mashayek et al. (2017) use a realistic regional simulation to argue that the mixing inferred from the DIMES TRE (Watson et al. 2013) was an order-of-magnitude larger than the in-situ diffusivity estimated from microstructure because the average diapycnal spreading of the tracer was dominated by a small fraction the tracer distribution that resided in regions of strong mixing near rough topography. Ruan and Ferrari (2021) derive exact evolution equations for the first and second tracer-weighted buoyancy moments (see Section 2a), which confirm Mashayek et al. (2017)'s speculation that the tracer's diapycnal variance grows like the tracer-weighted in-situ diffusivity. Ruan and Ferrari (2021) also identify a second "diapycnal stretching" term through which the bottom-enhancement of the buoyancy velocity in the SML further accelerates the diapycnal spreading of the tracer. Holmes et al. (2019) use a similar approach but include the effects of a sloping bottom boundary, and find that the diapycnal stretching in the SML is somewhat compensated for by a diapycnal contraction (or “boundary suppression") effect due to upwelling of relatively dense tracer in the BBL. However, since both of these analyses use extremely idealized models, it remains unclear to what extent diapycnal stretching affects tracers in realistic conditions.

Previous studies have speculated about the qualitative impacts of these stretching effects (Ledwell and Hickey 1995; Ledwell et al. 2000; Waterman et al. 2013), but did not quantify these impacts or the degree to which stretching effects are even included in their inverse models.

In this paper, we apply the buoyancy moments method in a quasi-realistic TRE simulation. We use tracer-weighted buoyancy moments diagnosed from the simulation to reinterpret the diapycnal downwelling and spreading observed in the Brazil Basin TRE (BBTRE; Ledwell et al. 2000 and St. Laurent et al. 2001) in the context of an emerging paradigm of bottom mixing layer control of the global abyssal circulation (Ferrari et al. 2016; McDougall and Ferrari 2017). We also provide guidance for the interpretation of past (e.g. Ledwell and Hickey 1995; Ledwell et al. 2004; Holtermann et al. 2012; Ledwell et al. 2016; Mackay et al. 2018; Visbeck et al. 2020) and future TREs that encounter topography.

2. Theory

We briefly review Ruan and Ferrari (2021)'s recently proposed framework for comparing tracer-based and microstructure-based mixing estimates, based on exact evolution equations for tracer moments in buoyancy space. The derivation begins with the conservation equations for tracer concentration c and buoyancy b,

$$\frac{\partial c}{\partial t} + \mathbf{u} \cdot \nabla c = \nabla \cdot (\kappa \nabla c) \tag{1}$$

$$\frac{\partial b}{\partial t} + \mathbf{u} \cdot \nabla b = \nabla \cdot (\kappa \nabla b), \tag{2}$$

where $\mathbf{u}$ is the velocity vector, $\nabla = \left(\frac{\partial}{\partial x}, \frac{\partial}{\partial y}, \frac{\partial}{\partial z}\right)$ is the gradient operator, and κ is an isotropic turbulent diffusivity (assumed to be the same for all tracers). Buoyancy, tracer concentrations, and velocity have been filtered on spatial and temporal scales larger than those associated with small-scale turbulence, and the filtered scalar fluxes are parameterized as an enhanced diffusive flux $\mathbf{F}_\phi = -\kappa \nabla \phi$, where the effective turbulent diffusivity is much larger than the molecular diffusivity. For simplicity of exposition, we here approximate density as a linear function of temperature; thus, density ρ, buoyancy b, and temperature T are all proportional and will be used interchangeably throughout: $b \equiv -g\frac{\rho}{\rho_0} \approx g\alpha T$, where ρ_0 is a reference density and α is the thermal contraction coefficient. (Salinity can be easily included as long as it is assumed to also be linearly proportional to density.)

a. Exact tracer-weighted buoyancy-moment models

In his classic paper, Taylor (1922) demonstrates that the growth rate of half the second moment of a 1D tracer distribution in physical space is exactly equal to its diffusivity. Ruan and Ferrari (2021) generalize this theory to the case of variable diffusivity in a stably stratified fluid by considering moments in buoyancy space. By cross-multiplying the passive tracer (1) and buoyancy (2) equations and integrating over a volume $\mathcal{V}$ containing the tracer (or bounded by insulating and impermeable boundaries), they derive straightforward and exact evolution equations for the first and second tracer-weighted buoyancy moments,

$$w_{\text{tracer}} \equiv \frac{\partial_t \overline{T}}{\overline{|\nabla T|}} = \frac{2\overline{\omega}}{\overline{|\nabla T|}} \quad \text{and} \tag{3}$$

$$\underbrace{\frac{1}{2}\frac{\partial_t \overline{\left(T-\overline{T}\right)^2}}{\overline{|\nabla T|^2}}}_{\substack{\kappa_{\text{tracer}} \\ \text{(spreading)}}} = \underbrace{\frac{\overline{\kappa|\nabla T|^2}}{\overline{|\nabla T|^2}}}_{\substack{\kappa_{\text{Taylor}} \\ \text{(diffusion)}}} + \underbrace{2\frac{\overline{\omega' T'}}{\overline{|\nabla T|^2}}}_{\substack{\kappa_{\omega} \\ \text{(stretching)}}}, \tag{4}$$

respectively, where overlines denote the tracer-weighted average, $\overline{\star} \equiv \frac{\int_{\mathcal{V}} \star\, c\, \mathrm{d}V}{\int_{\mathcal{V}} c\, \mathrm{d}V}$; primes denote variations from the tracer average, $\star' \equiv \star - \overline{\star}$; and $\omega \equiv \nabla \cdot (\kappa \nabla T)$ is the in-situ buoyancy velocity, which is the magnitude of the diapycnal velocity through buoyancy space (e.g. Marshall et al. 1999). We have taken an additional step of converting to physical velocity and diffusivity units by normalizing by the appropriate tracer-weighted powers of the buoyancy gradient.

b. Interpreting the tracer-weighted buoyancy moments

Consider the extreme example of a tracer distribution $c_{i,j}$ consisting of two infinitesimal patches at locations $\mathbf{x}_i$ and $\mathbf{x}_j$ and with equal mass,

$$c_{i,j}(\mathbf{x}) = \delta(\mathbf{x}_i) + \delta(\mathbf{x}_j), \tag{5}$$

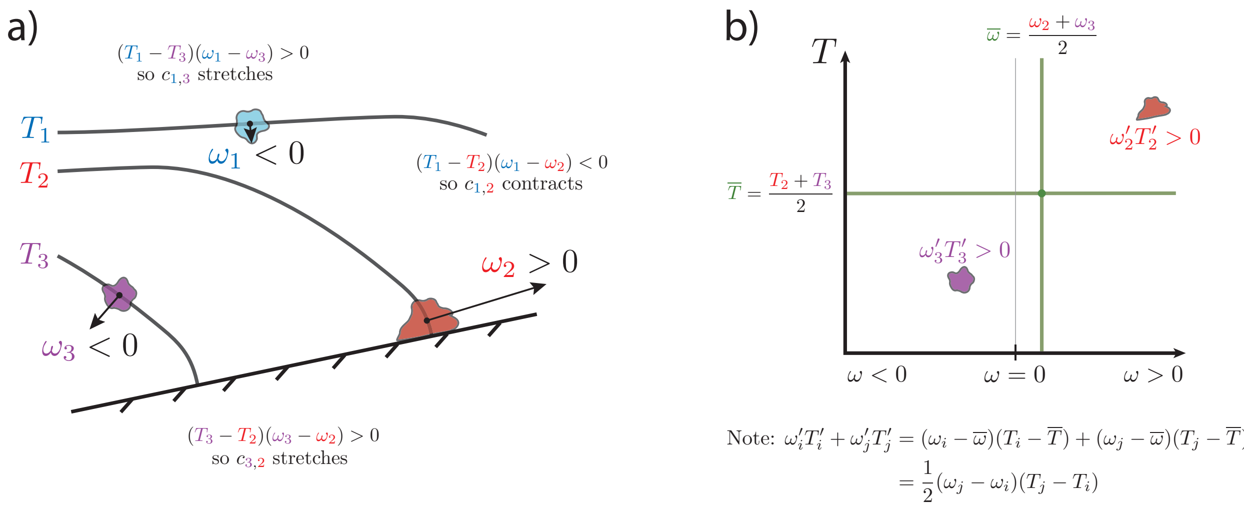

FIG. 1. Examples of diapycnal stretching and contraction of bi-modal tracer distributions (eq. 5) in physical space (a) and in (ω, T) space (b). a) The three tracer distributions $c_{1,3}$, $c_{1,2}$, and $c_{3,2}$ experience diapycnal spreading or contraction effects due to temperature and buoyancy velocity differences. Gray lines show the equally-spaced temperature surfaces corresponding to the three tracer patches. Arrows represent the magnitude of the buoyancy velocity ω and are oriented normal to temperature surfaces. b) PDF of contributions to $c_{3,2}$'s net diapycnal stretching effects both tracer patches. Olive lines mark the average buoyancy velocity and temperature of the tracer.

where $\delta(\mathbf{x})$ is the Delta function. The evolution of the first moment (3) is simply given by the twice the average buoyancy velocity of the two patches,

$$\partial_t \overline{T} = 2\overline{\omega} = \omega_i + \omega_j, \tag{6}$$

where we use the shorthand $\phi_k \equiv \phi(\mathbf{x}_k)$. The evolution of the centered second moment (4), is given by

$$\frac{1}{2}\partial_t \overline{\left(T - \overline{T}\right)^2} = \overline{\kappa |\nabla T|^2} + \frac{1}{2}\Delta\omega \Delta T, \tag{7}$$

where $\Delta\omega \equiv \omega_j - \omega_i$ and $\Delta T \equiv T_j - T_i$ are buoyancy velocity and temperature differences between the two patches, respectively. While the first moment tendency is simply given by the average of the two patches' tendencies, the centered second moment tendency includes an additional non-linear interaction term. If the warmer patch upwells faster than the colder patch ($\Delta\omega\Delta T > 0$), this term drives diapycnal stretching (e.g. $c_{1,3}$ and $c_{3,2}$ in Figure 1); conversely, $\Delta\omega\Delta T < 0$ corresponds to diapycnal contraction (e.g. $c_{1,2}$ in Figure 1).

A corollary of (7) is the fact that estimates of the in-situ diffusivity are most reliable when the injected tracer distribution is compact in buoyancy space (i.e. $\Delta T \approx 0$), supporting the practice of localized TREs. Even for an initially compact tracer injection with $\Delta\omega\Delta T \simeq 0$, diapycnal stretching effects may become significant over time as ΔT increases due to diapycnal diffusion; on the other hand, while isopycnal stirring does not increase ΔT (by definition), it can increase $\Delta\omega$ by distributing tracer into regions with varying buoyancy velocities. While the former effect is likely to be well represented in 1D advection-diffusion models used to interpret TRE data, the latter is not.

3. Numerical methods overview: simulated Tracer Release Experiments

We configure the MITgcm to simulate mixing-driven flow in the BBTRE region (Figure 2a). Inspired by sloping bottom boundary layer theory (reviewed by Garrett et al. 1993), the system is solved in a coordinate frame aligned with the mean MAR slope, as described in detail in a companion manuscript (Drake et al. 2021, in prep.) and summarized in Appendix A. The simulation is forced only by bottom-enhanced turbulent mixing, which controls diabatic tracer upwelling and spreading and is thought to provide much of the available potential energy that drives sub-inertial abyssal flows. Sub-grid scale turbulent fluxes of a filtered tracer ϕ are parameterized as down-gradient turbulent diffusion, $\mathbf{F}_\phi \approx -\kappa\nabla\phi$, whose magnitude is controlled by a turbulent diffusivty κ that increases exponentially towards the seafloor (Figure 2b),

$$\kappa(x, y, z) = \kappa(z; d) = \kappa_{\text{BG}} + \kappa_{\text{BOT}} \exp\left(\frac{z-d}{h}\right),$$

and is fit to the mean height-above-bottom microstructure profile in the region according to Callies (2018), with $\kappa_{\text{BOT}} = 1.8\times10^{-3}\,\text{m}^2/\text{s}$, $\kappa_{\text{BG}} = 5.2\times10^{-5}\,\text{m}^2/\text{s}$, and $h = 230\,\text{m}$.

After spinning up the flow to a quasi-equilibrium state at $t = 5000$ days, we release three Gaussian blobs of tracer,

$$c_n(x, y, z, t=0) = c_0 \exp\left\{-\left(\frac{(x-x_0)^2}{\sigma_x^2} + \frac{(y-y_0)^2}{\sigma_y^2} + \frac{(z-z_n)^2}{\sigma_z^2}\right)\right\}, \tag{8}$$

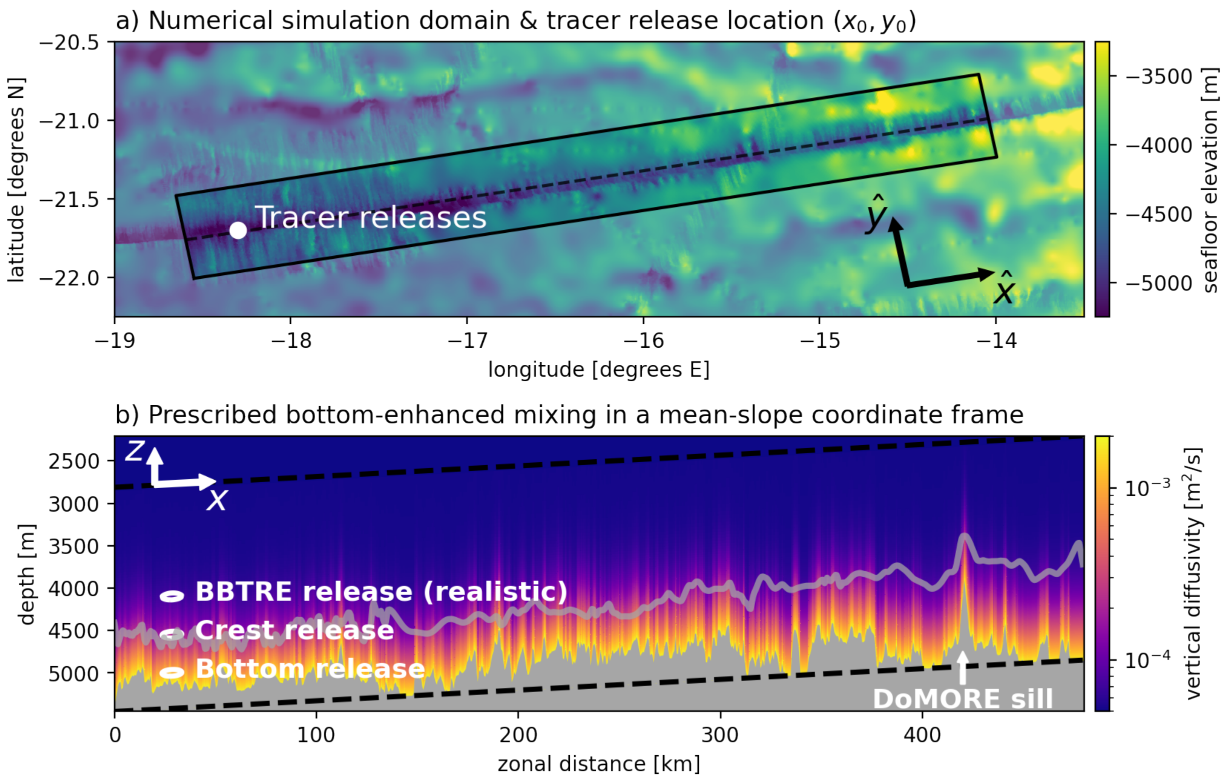

Fig. 2. Numerical model configuration: domain geometry, prescribed forcing, and key features. a) Rectangular domain (solid lines) centered along the BBTRE canyon thalweg (dashed line) and interpolated onto locally-tangent cartesian coordinates $(\hat{x}, \hat{y})$. b) Prescribed bottom-enhanced mixing (colors) along the canyon thalweg (grey shading). Dashed black lines show the domain limits in the slope-native coordinate frame (x, z). The transparent grey line shows the average height of the canyon crests, which rise 500 m to 1000 m above the thalweg (its deepest section). White dots/contours show the locations of the simulated tracer releases. The location of the prominent Dynamics of the Mid-Ocean Ridge Experiment (DoMORE– see Clément et al. 2017) sill is shown for reference.

with horizontal widths of $\sigma_x = \sigma_y = 10\,\mathrm{km}$, a thickness $\sigma_z = 100\,\mathrm{m}$, and horizontal release coordinates (x_0, y_0) corresponding to the location where the tracer was released in the BBTRE (18.3 °W, 21.7 °S) (Figure 2). The tracers are released at three different heights z_n corresponding to distinct dynamically interesting regimes: far above the topography, $z_{\mathrm{BBTRE}} - d(x_0, y_0) = 1050\,\mathrm{m}$ above the seafloor (actual BBTRE release location; hereafter the BBTRE tracer); roughly at the height of the canyon crests, $z_{\mathrm{Crest}} - d(x_0, y_0) = 600\,\mathrm{m}$ (Crest); and within the thick BBL of the canyon trough, $z_{\mathrm{Bottom}} - d(x_0, y_0) = 150\,\mathrm{m}$ (Bottom). We follow the evolution of these released tracers until $t_f = 440$ days after release, roughly corresponding to the first survey in the BBTRE at 14 months.

4. Results

a. Temporal evolution of the released tracer distributions

Within the first few eddy turnover timescales, the released tracer blobs are stirred into a web of filaments along isopycnals by submesoscale eddies (e.g. Figure 3). While the BBTRE and Crest tracers are released well above the canyon thalweg (its deepest section; Figure 2a), vigorous along-ridge mean flow (Figure 4) and isopycnal stirring by submesoscale eddies spread them to shallower regions (Figure 5).

The tracers are diffused diapycnally by the prescribed bottom-enhanced turbulent mixing (e.g. Figure 5b,d). For the BBTRE tracer, which mostly remains well above the bottom, its distribution in temperature space remains reasonably Gaussian (Figure 5d), reminiscent of diffusion with a constant diffusivity and in the absence of boundaries; for the Crest and Bottom tracers, however, the tracer distributions depart significantly from Gaussianity (Figure 5h,l), suggesting the importance of variations in the diffusivity or boundary effects. Most notably, the Bottom tracer develops a bi-modal distribution in temperature space as some of the tracer spills over the minor sill at $x = 120$ km and crosses the $T = 0.7\,°\mathrm{C}$ surface (Figure 5j, l). By the end of the experiment at 440 days, most of the Bottom tracer has spilled over the sill and its bi-modal distribution collapses onto a single, warmer, peak. While only the Bottom tracer exhibits a tracer-weighted diapycnal motion that is discernible by visually inspecting the tracer distributions in temperature space, the BBTRE and Crest tracers do exhibit slow mean diapycnal downwelling and upwelling, respectively.

b. Diapycnal interior downwelling and boundary upwelling driven by bottom-enhanced mixing

As described in Section 2a, the mean diapycnal motion of the tracer is directly driven by the tracer-weighted buoyancy velocity $\overline{\omega} \equiv \overline{\nabla \cdot (\kappa \nabla T)}$ (eq. 3). In the SML, well above the seafloor, the bottom-enhancement of the diffusivity κ dominates the buoyancy velocity, resulting in diapycnal downwelling, $\omega < 0$. Closer to the seafloor, the temperature flux must vanish to satisfy the insulating bottom boundary condition, resulting in vigorous diapycnal upwelling, $\omega > 0$, in the BBL.

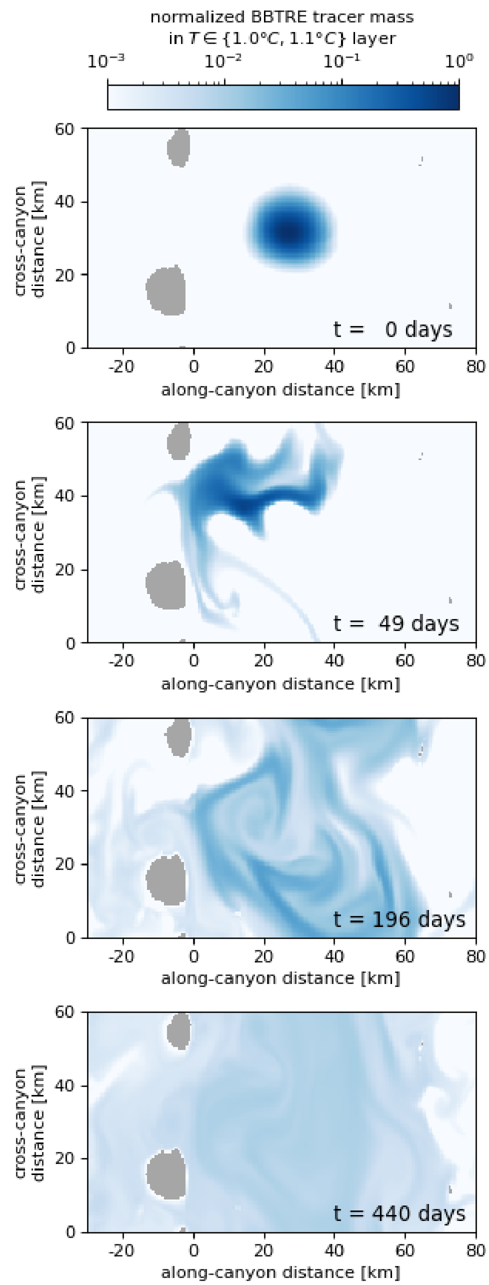

FIG. 3. Instantaneous snapshots of the BBTRE tracer mass, vertically-integrated over the {1.0 °C, 1.1 °C} temperature layer, and normalized by the maximum initial tracer mass. The grey shading represents two major topographic obstacles, where the temperature layer in-crops.

The BBTRE tracer, which is released in the SML, exhibits diapycnal downwelling throughout the experiment (Figure 6c), consistent with the above phenomenology. The magnitude of downwelling, however, is modulated by a 45-day damped oscillation due to along-ridge advection by a mean-flow

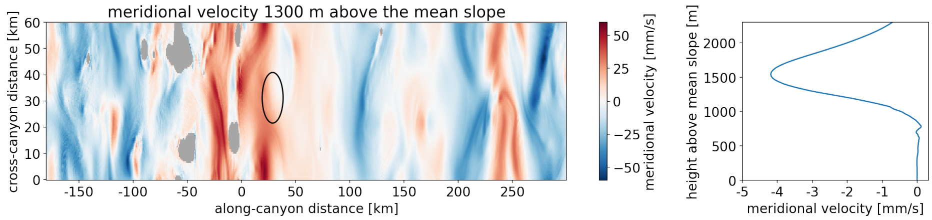

FIG. 4. (a) Cross-canyon meridional velocity 1300 m above the mean slope, i.e. at the release height of BBTRE tracer. The black contour shows the initial extent of the tracers, which is released in an anomalously northward flow. (b) Same as a), but averaged across the whole domain.

of speed $U \approx 15\,\mathrm{mm/s}$ (Figure 4a) across a periodic domain of width $L_y = 60\,\mathrm{km}$, such that the tracer aliases the roughly sinusoidal trough-crest topography on a timescale of $\tau = L_y/U \approx 45\,\mathrm{days}$. This modulation is damped over time as the tracer spreads isopycnally and spans a region wider than the typical trough-crest separation (Figure 5a).

In the first 100 days, interpreting the mean diapycnal sinking of the BBTRE tracer is straightforward: the entire tracer distribution experiences a negative buoyancy velocity and so the tracer sinks diapycnally (Figure 6c), i.e. $\overline{\omega} \approx \overline{\omega_{<0}}$, where we define:

$$\overline{\omega_{<0}} \equiv \frac{\int_{\mathcal{V}_{\omega<0}} \omega\, c\, \mathrm{d}V}{\int_{\mathcal{V}} c\, \mathrm{d}V} \tag{9}$$

as the strictly downwelling buoyancy velocity. While this strictly downwelling contribution to the tracer-weighted buoyancy velocity increases slightly over the remainder of the experiment as the tracer sinks towards larger diffusivities, sufficient tracer is entrained into the BBL that a strictly upwelling contribution $\overline{\omega_{>0}}$ (similarly defined) grows at an even faster rate, such that the net diapycnal sinking of the tracer weakens over the last few hundred days of the experiment (Figure 6c).

At the other extreme, the Bottom tracer is released entirely in the BBL and thus upwells vigorously upon release, with $\overline{\omega} \approx \overline{\omega_{>0}}$ (Figure 6g). As some of the tracer eventually spreads into the SML above and the strictly negative contribution $\overline{\omega_{<0}}$ grows, the net upwelling of the tracer weakens over time[3].

[3]The Bottom tracer is released near the bottom of a weakly stratified depression along the canyon thalweg, and its average stratification increases dramatically over the first 200 days (Figure 6a,b). Thus, the early diapycnal upwelling and spreading is enhanced when converting to physical space because the buoyancy surfaces are on average much further apart than they are later on (see normalization in equations 3 and 4).

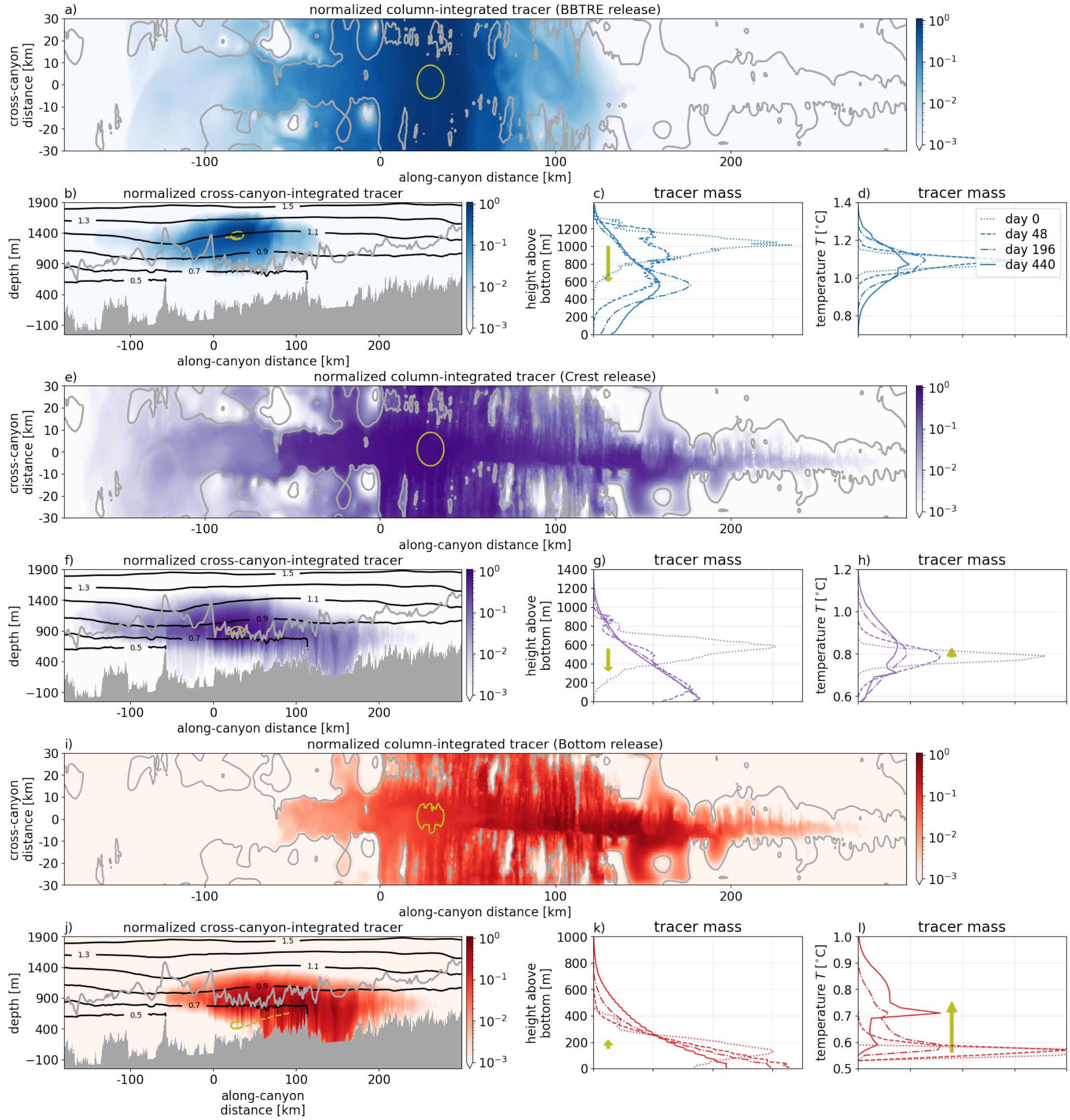

FIG. 5. Temporal evolution of the tracer distributions in Cartesian, height-above-bottom, and temperature coordinates for the BBTRE (a-d; blues), Crest (e-h; purples), and Bottom releases (i-l; reds). (a,e,i) Slope-normal column-integrated tracer concentrations and (b,f,j) cross-canyon-integrated tracer concentrations, normalized by their maximum value (logarithmic scale). Grey contours in (a,e,f) show two representative isobaths of ocean depth $\hat{d}(\hat{x}, \hat{y})$. Black lines in (b,f,j) show equally-spaced cross-canyon-averaged temperature surfaces. Tracer distributions in (c,g,k) height-above-bottom and (d,h,l) temperature coordinates, normalized by their maximum initial values (linear scale). Olive contours show the 10% contour for the initial tracer distribution; olive dashed and arrows show the temporal evolution of the tracer's center of mass (first moments).

The Crest release is perhaps the most interesting: at first, the Crest tracer is in the SML far above the canyon thalweg and thus downwells similarly to the BBTRE tracer; after roughly $\tau = 46$ days, however, enough of the Crest tracer is advected into the BBLs along the rim of the canyon and the surrounding hills that the strictly upwelling component wins out and the tracer begins upwelling in the net (Figure 6e). Over the last few hundred days of the experiment, the weak net upwelling of the tracer is the small residual of a substantial compensation between strictly upwelling and strictly downwelling contributions.

By plotting the evolution of the temperature moment tendency as a function of the tracer-weighted height-above-bottom, we gain a qualitative sense of the height-above-bottom structure of the in-situ buoyancy velocity (Figure 7a). As the three tracers' centers of mass drift over time, their average buoyancy velocities trace out a diapycnal downwelling that increases rapidly towards the bottom in the SML (Figure 7a, blue). Below about 300 m, however, this downwelling gives way to upwelling (Figure 7a, purple) which intensifies the closer the tracer is to the bottom (Figure 7a, red).

In practice, however, *instantaneous* measurement of the tracer-weighted temperature (or temperature variance) tendency is infeasible. Instead, practical methods are akin to estimating the time-average of the right hand-side of eq. 3 (or eq. 4) from finite differencing of the tracer-weighted volume-averaged temperature (or temperature variance)

$$\frac{1}{t_1 - t_0} \int_{t_0}^{t_1} \partial_t \overline{T}\, \mathrm{dt} = \frac{\overline{T}(t_1) - \overline{T}(t_0)}{t_1 - t_0} = \frac{1}{t_1 - t_0} \int_{t_0}^{t_1} 2\overline{\omega}\, \mathrm{dt} \tag{10}$$

between observational surveys at t_0 and t_1, typically representing two separate cruises separated by multiple months[4] (Watson et al. 2013; Ledwell et al. 2000). Alternatively, a linear fit through multiple surveys of $\overline{T}(t)$ can be interpreted as an estimate of *twice* the time-mean tracer-weighted buoyancy velocity. Ledwell et al. (1998) follow this general approach but incorrectly omit the factor of two, which would have brought their tracer-based mixing estimates more in-line with St. Laurent and Schmitt's (1999) in-situ mixing estimates).

Taking t_0 at release and $t_1 = 14$ months, as in BBTRE, the changes in the tracers' first moments still reveal the structure of abyssal mixing layer transformations, albeit at very low resolution: slow

[4] With this method, the number of distinct time-mean buoyancy velocity estimates produced by all pairs of the n surveys of $\overline{T}(t_n)$ is $\binom{n}{2} = \frac{n!}{2(n-2)!} = \frac{n(n-1)}{2} \propto n^2$, potentially providing insight into the temporal variability of mixing rates on various timescales. However, most past studies typically only consider either the n pairs that include the release as one endpoint (e.g. Watson et al.'s 2013 estimates of the second moments) or the n pairs of consecutive surveys (e.g. Ledwell et al.'s 1998's estimates of second moments).

sinking in the SML, rapid upwelling in the BBL, and slow upwelling in between the two (Figure 7a, stars). These promising results suggest that equation (10) offers a novel practical method for estimating buoyancy velocities from TREs based on Ruan and Ferrari (2021)'s tracer-weighted buoyancy moment equations, with the caveat that we have assumed perfect spatial information at instantaneous surveys at both t_0 and t_1.

Watermass transformations provide a helpful reference for contextualizing the magnitude and vertical structure of tracer-weighted velocities. In Appendix B, we convert the height-above-bottom (or η) structure of watermass transformations into an effective vertical velocity versus η-profile (see Appendix B),

$$\overline{W}^{T}(\eta) \equiv \frac{\sin\theta}{L_y}\frac{\partial}{\partial\eta}\overline{\mathcal{E}}^{T}(\eta). \tag{11}$$

This metric reveals that vigorous upwelling of $\mathcal{O}(4\times10^{-5}\,\mathrm{m/s})$ is on average confined to the 40 m-thick BBL, largely compensated by downwelling an order of magnitude weaker and broader in the SML above (Figure 8b-d, grey lines). This would superficially seem to be inconsistent with the tracer diagnostics, which exhibit weaker BBL upwelling that extends an order of magnitude higher above the bottom.

The key to reconciling the two diagnostics is that the tracer distributions, while initially compact, rapidly spread in η-space (Figure 5c,g,k). To demonstrate the effect of this spreading on the tracer diagnostics, we convolve the vertical velocity versus η-profile (11) with smoothing tracer kernels of different shapes and widths (Figure 8a),

$$\overline{W}(\eta) \approx \int_{-\infty}^{\infty}\mathcal{K}(\eta-\eta')\overline{W}^{T}(\eta')\,\mathrm{d}\eta'. \tag{12}$$

Tracer kernels with widths less than the thickness of the BBL accurately reproduce its η-structure, while thicker kernels begin smearing the BBL and SML together, reducing both of their magnitudes and elevating the apparent interface between them (Figure 8b,c,d). This smearing effect is particularly dramatic for exponential kernels with thick tails, which reasonably approximates the shapes of the Crest and Bottom tracers for most of the experiment (Figure 5g,k). Indeed, convolving the vertical velocity η-profile with exponential kernels of the same approximate width of these tracers reasonably reproduces the tracer-diagnosed η-structure of the buoyancy velocity (Figure 8d). By contrast, the buoyancy velocity experienced by the BBTRE tracer is not as severely convoluted

(Figure 8b-d) because it neither spreads as rapidly nor does it feel much of the compensating BBL upwelling (Figure 5c).

c. Bottom-enhanced diapycnal tracer spreading

Over the course of the experiment, all three tracers spread across isopycnals on average. As anticipated from the prescribed bottom-enhanced diffusivity profile: the closer a tracer is released to the bottom, the faster it spreads (Figure 7a; stars). However, this time-mean view obscures surprisingly large temporal variability (Figure 6f,h). This tendency is particularly dramatic for the Bottom tracer, which experiences extremely rapid diapycnal spreading in the first 150 days but, by day 350, stops spreading entirely and even begins temporarily *contracting* in buoyancy space (Figure 6h)! The interpretation of diapycnal tracer spreading is more subtle than that of the mean diapycnal motion of the tracer, since two separate terms contribute to spreading: the tracer-weighted effective diffusivity κ_{Taylor} and diapycnal stretching κ_ω (eq. 4). The contribution from the tracer-weighted effective diffusivity is familiar from Taylor (1922)'s classic derivation, and is reasonably well approximated by the tracer-weighted in-situ diffusivity $\overline{\kappa}$ since correlations between the diffusivity and the squared temperature gradients are relatively small (Figure 6d,f,h),

$$\kappa_{\text{Taylor}} \equiv \frac{\overline{\kappa|\nabla T|^2}}{\overline{|\nabla T|^2}} \approx \overline{\kappa}. \tag{13}$$

This contribution to diapycnal spreading from the tracer-weighted diffusivity remains roughly constant in time, aside from an initial transient as the tracer spreads towards shallower topographic features (Figures 7b). In contrast, the diapycnal stretching effect drives the substantial temporal variability in the diapycnal spreading experienced by the tracers (Figure 6d,f). Depending on the instantaneous distribution of the tracer, this term can vary substantially both in magnitude and sign, either amplifying the tracer-weighted diffusivity by up to 100% or off-setting it entirely (Figure 7b,c; at 40 and 400 days, respectively).

d. Disentangling diapycnal stretching and contraction effects

Motivated by the bi-modal example in Section b, we decompose the diapycnal stretching term κ_ω by binning its contributions in (ω, T) space (Figure 9, as in Figure 1b), i.e. by decomposing the volume integral into a sum over sub-volumes:

$$\frac{\kappa_\omega}{\kappa_{\text{Taylor}}} = \sum_{i,j} \int_{\mathcal{V}_{\{\omega_i\}\cap\{T_j\}}} \frac{2\omega' T' c}{\mathcal{M}\,\overline{|\nabla T|^2}\,\kappa_{\text{Taylor}}}\,\mathrm{d}V, \tag{14}$$

where $\mathcal{M} \equiv \int_{\mathcal{V}} c\,\mathrm{d}V$ is the total tracer mass and the intersection of subsets $\{\omega_i\}$ and $\{T_j\}$ correspond to distinct sub-volumes $\mathcal{V}_{\{\omega_i\},\{T_j\}}$ of the tracer distribution, defined by their (ω, T) characteristics. Figure 9 shows heatmaps of the contributions from relatively narrow (ω', T') bins as well as the summed contributions from each of the quadrants delineated by the respective signs of ω' and T'. In (14) and throughout this section, we normalize by the total effective diapycnal diffusion κ_{Taylor} to quantify the relative importance of the unconventional stretching effects compared to the more conventional diapycnal diffusion; for example, $\kappa_\omega/\kappa_{\text{Taylor}} = 100\%$ implies stretching doubles the diffusive spreading rate while $\kappa_\omega/\kappa_{\text{Taylor}} = -100\%$ implies net stretching is sufficiently negative (i.e. contraction) to exactly offset the diffusive spreading.

We begin by exploring why the BBTRE tracer experiences very little net diapycnal stretching, in contrast to the idealized SML simulation of Ruan and Ferrari (2021). At day 100 (Figure 9a), for example, the tracer is diapycnally stretched ($\overline{\omega' T'} > 0$) by an additional $23\%\kappa_{\text{Taylor}}$ (hereafter dropping the κ_{Taylor} for convenience) as relatively cold tracer relatively downwells ($T' < 0$, $\omega' < 0$) and relatively warm tracer relatively upwells ($T' > 0$, $\omega' > 0$). This stretching of 23% is so far consistent with Ruan and Ferrari (2021)'s idealized result of 18% additional stretching. However, a very small amount of cold tracer has made it close enough to the seafloor to be entrained in the BBL, where it upwells vigorously and results in a contraction effect of −9% which, supplemented by an additional −2% contraction from warm downwelling tracer, results in a reduction of the net diapycnal stretching to only 23% − 11% = 12%. By day 440, this patch of tracer is pulled further towards the bottom and its stretching effect grows to 69%, but is offset by an even larger diapycnal contraction of −76% in the BBL (Figure 9b); combined, these diapycnal stretching effects have a negligible effect of reducing diapycnal spreading by only −6%, in contrast to the continued strengthening of stretching effects[5] predicted by Ruan and Ferrari (2021).

At the other extreme, we aim to understand how the Bottom tracer undergoes first a large net diapycnal stretching effect and then an even larger net diapycnal contraction effect. Over the

[5]Ruan and Ferrari (2021) acknowledge stretching may eventually be limited by boundary suppression (as in Holmes et al. 2019), but do not elaborate on its relative timing or magnitude.

first 100 days, most of the tracer upwells in the BBL and warms (Figure 6g). Some of the warmest tracer remains in the BBL, where its upwelling drives a substantial diapycnal stretching of 91% (Figure 9c). However, part of this warm branch of the tracer is entrained into the SML, where its downwelling drives a largely compensating diapycnal contraction effect of −80%. The relatively cold patch of tracer that is left behind contributes a stretching of 41% − 15% = 26%, dominated by its relatively slow upwelling ($\omega > 0$ but $\omega' < 0$), bringing the net diapycnal stretching to 91% − 80% + 26% = 37%. By day 440, however, both modes of the tracer distribution (Figure 5l) drive large diapycnal contraction effects: −98% due to cold upwelling upstream of the sill and −101% due to warm downwelling downstream of the sill (Figures 5j,l 9d). Diapycnal stretching of 93% from the other quadrants offset about half of this diapycnal stretching effect, but the net diapycnal contraction of −106% still overwhelms the spreading due to the in-situ diffusivity, causing the Bottom tracer to temporarily contract in buoyancy space—countering conventional intuition about the average effects of down-gradient diapycnal diffusion.

5. Discussion and Conclusion

By applying Ruan and Ferrari (2021)'s buoyancy-moment diagnostics to our quasi-realistic regional simulation of mixing-driven abyssal flows (described in detail in companion manuscript, Drake et al. 2021, in prep), we confirm the qualitative results of Holmes et al. (2019)'s idealized analysis of the BBTRE release in the SML: over time, boundary suppression in the BBL almost exactly compensates for vertical stretching in the SML, such that the net diapycnal spreading of the BBTRE tracer coincidentally provides a reasonably accurate (±20%) estimate of the tracer-weighted in-situ diffusivity (Figure 6d). These simulation results are supported by a recent re-analysis of the BBTRE observations, which reveal a similarly negligible diapycnal stretching effect of $< 5\% \kappa_{\text{Taylor}}$ (Figure 6d; Ledwell, personal communication). Quantitatively, however, the diapycnal spreading we simulate for the BBTRE tracer is smaller than the observed spreading by a factor of 2 (Figures 6d, 11), suggesting either the microstructure measurements we use to tune the prescribed diffusivity profile are biased low or our simulation is missing other unknown tracer dispersion processes. This is consistent with Ledwell (in prep)'s inversion of a 1D advection-diffusion model, which produced optimal diffusivities about twice as large as the microstructure's sample-mean. Our results are also consistent with the conclusion of the companion manuscript (Drake et al. 2021, in prep.), which shows that biases in the simulated flows and stratification of the BBTRE fracture zone canyon also suggest the imposed microstructure mixing rates may be biased low by a factor of roughly 2. These BBTRE-specific results are consistent with the broader observational literature, which unanimously finds that mixing rates estimated from TREs are larger than those suggested by co-located microstructure measurements (Ruan and Ferrari 2021).

In contrast to the BBTRE release, we find that for near-bottom tracers diapycnal stretching/contraction effects can be of either sign (depending on the tracer distribution) and of comparable magnitude to the tracer-weighted in-situ diffusivity, $|\kappa_\omega| \sim \kappa_{\text{Taylor}} \simeq \overline{\kappa}$ (Figure 6h). Our simulations demonstrate that three-dimensional eddies and topographic effects have a leading order effect on diapycnal tracer spreading, as tracer distributions are chaotically transported in and out of regions of vigorous mixing. Unsurprisingly, diapycnal stretching and contraction effects are much stronger—and more variable—in our three dimensional flows over rough topography than the already substantial effects reported by Holmes et al. (2019) for two-dimensional tracer transport under one-dimensional boundary layer dynamics with parameterized isopycnal eddy stirring. For our Bottom tracer release, for example, diapycnal stretching amplifies diapycnal spreading by $O(100\%\kappa_{\text{Taylor}})$ in the first few dozen days of the simulation but suppresses diapycnal spreading by $O(-100\%\kappa_{\text{Taylor}})$ for the last few dozen days (Figures 6h; 7c).

Given that rough topography generally implies strong bottom-enhanced diapycnal mixing (Polzin et al. 1997; Waterhouse et al. 2014), which is in turn thought to incite bottom mixed layer eddies (Callies 2018; Wenegrat et al. 2018; Ruan and Callies 2020), significant diapycnal stretching and contraction effects are to be expected near sloping rough topography in the abyss, such as along the global mid-ocean ridge system (Ledwell et al. 2000; Thurnherr et al. 2005, 2020) and within continental slope canyons (Nazarian et al. 2021; Hamann et al. 2021; Alberty et al. 2017). In these regions, unlike for interior ocean releases such as BBTRE, tracer-based estimates of mixing rates must take into account the three-dimensional history of the tracer distribution's evolution.

It has long been appreciated that the interpretation of tracer spreading near topography requires greater care because of enhanced boundary mixing and hypsometric effects (e.g. Ledwell and Hickey 1995). Attempts to modify the conventional 1D model to include these boundary effects are varied: by separating the tracer distribution into "boundary" and "interior" regions (Ledwell and Hickey 1995; Ledwell et al. 2016), by allowing vertical structure in the diffusivity profile (Ledwell et al. 2000), or by extending the 1D model to a 2D (Watson et al. 2013) or 3D (Mackay et al. 2018) model to account for lateral transport into and out of regions of strong mixing. However, the ad-hoc derivations of these models render them difficult to interpret and compare, suggesting a complementary role for the more exact buoyancy-moment approach (Ruan and Ferrari 2021).

Mesoscale/submesoscale-resolving regional simulations of TREs are now feasible thanks to exponential increases in computational power (Tulloch et al. 2014; Mashayek et al. 2017; Ogden et al., in prep; this study) and have been used *a posteriori* to help interpret observations and explain differences between mixing rates inferred from TREs and microstructure profiles. However, such simulations have not yet been used to evaluate (or improve upon) operational methods for comparing tracer and microstructure observations, such as by using a "perfect model" framework in which simulated tracer observations are inverted in an attempt to recover the prescribed "true" diffusivity field. Similarly, *a priori* or real-time numerical simulations could be used to inform future TRE sampling strategies (current best practice is to roughly estimate horizontal transport from real-time velocity estimates from ADCPs or altimetry; Messias and Ledwell, personal communication). To our knowledge, this has not yet been done, with the notable exception of the *Bottom Boundary Layer Turbulence and Abyssal Recipes* team (BLTTRE; NSF Award #1756251), who are using TRE simulations to inform the experiment's planning and sampling strategies.

While our results suggest that estimates of in-situ diffusivity profiles from observations of a tracer's *second* buoyancy moment may be corrupted by complicated diapycnal stretching processes (Figure 7c; consistent with Holmes et al. 2019), they also suggest that the *first* buoyancy moment provides a more robust and straight-forward estimate of the tracer-weighted in-situ turbulent buoyancy flux convergence (or buoyancy velocity ω; Figure 7a). However, if the width of the tracer distribution is longer than the scale of flow variations, or if the tails are sufficiently thick, even the first moment diagnostics can be a misleading combination of upwelling and downwelling flows (Figure 8). Nevertheless, as long as a sizable fraction (here $\gg \overline{W}^T_{\text{SML}}/\overline{W}^T_{\text{BBL}} \approx 10\%$; Figure 8) of the tracer remains in the BBL, the change in the first tracer-weighted buoyancy-moment is likely to provide at least a reasonable lower-bound estimate of the average in-situ buoyancy velocity in the BBL (Section 2b). This is a promising result in light of the ongoing BLTTRE, which aims to provide the first in-situ estimates of BBL upwelling. Short-term surveys, when the tracer distribution is still relatively compact (e.g. from a dye release experiment)—may be interpreted as lower bound estimates of BBL upwelling—while long-term surveys—when the tracer roughly equally occupies the BBL and SML—may be interpreted as estimates of net upwelling. Combined, these two estimates could constrain the strength of the amplification factor, the ratio of strictly upwelling transport in the BBL to net upwelling, which is predicted by theory to be much larger than 1 (Ferrari et al. 2016; McDougall and Ferrari 2017; Callies 2018; Holmes and McDougall 2020). In combination with previous observations of tracer-weighted diapycnal sinking in the SML above rough topography (Ledwell et al. 2000), observations of vigorous tracer-weighted diapycnal upwelling in the BBL would be compelling direct evidence for the emerging paradigm of bottom mixing layer control of the abyssal meridional overturning circulation (Ferrari et al. 2016; de Lavergne et al. 2016a; Callies 2018; Callies and Ferrari 2018; Drake et al. 2020; Drake et al., companion paper in prep).

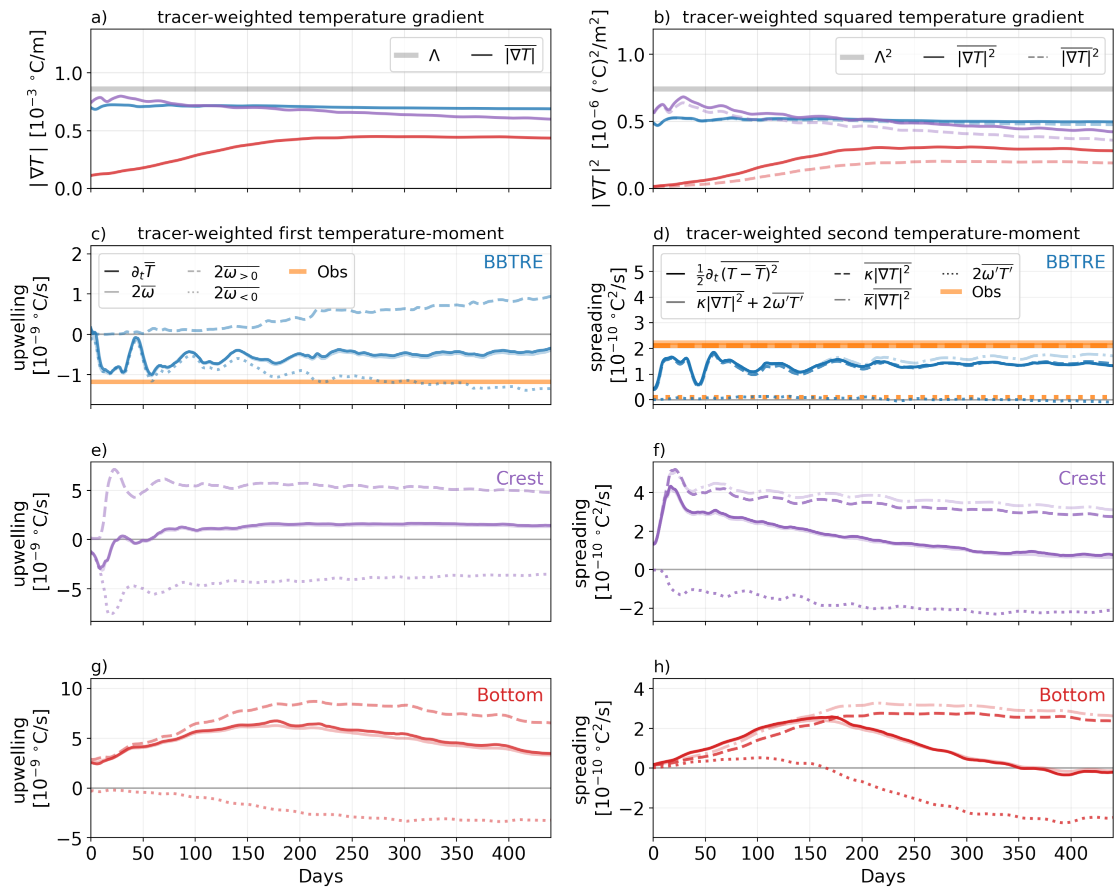

FIG. 6. Decomposition of the first and second tracer-weighted temperature moment tendencies, i.e. the rates of diapycnal motion and spreading, in terms of their driving mixing processes. The realistic BBTRE release is shown in blue, the Crest release in purple, and the Bottom release in red. (a-b) show the temporal evolution of the tracer-weighted stratification and stratification squared, with the background stratification $\Lambda \equiv \frac{dT_b}{d\hat{z}}$ for reference (see Appendix A). (c-h) show the temporal evolution of the first and second moment tendencies (opaque solid lines) which are visually indistinguishable from the sum of the contributing mixing processes (transparent solid lines; demonstrating that spurious numerical mixing is negligible), as described by the left- and right-hand-sides of equations (3), $\partial_t \overline{T} = 2\overline{\omega}$, and (4), $\frac{1}{2}\partial_t \overline{(T-\overline{T})^2} = \overline{\kappa|\nabla T|^2} + 2\overline{\omega' T'}$, respectively. Orange lines in (c,d) show the time-averaged BBTRE moment tendencies estimated from observations, where the κ used in the right-hand-side terms is a height-above-bottom profile estimated from an inverse model (Ledwell et al. 1998, revised by Ledwell, in prep). (c,e,g) Dashed and dotted lines show the contributions from strictly upwelling and strictly downwelling regions, respectively. (d,f,h) Dashed lines show the contribution from tracer-weighted in-situ diffusion κ_{Taylor} (approximately equal to the tracer-weighted in-situ diffusivity $\overline{\kappa}$; dash-dotted lines) and dotted lines show the contribution from diapycnal stretching κ_ω.

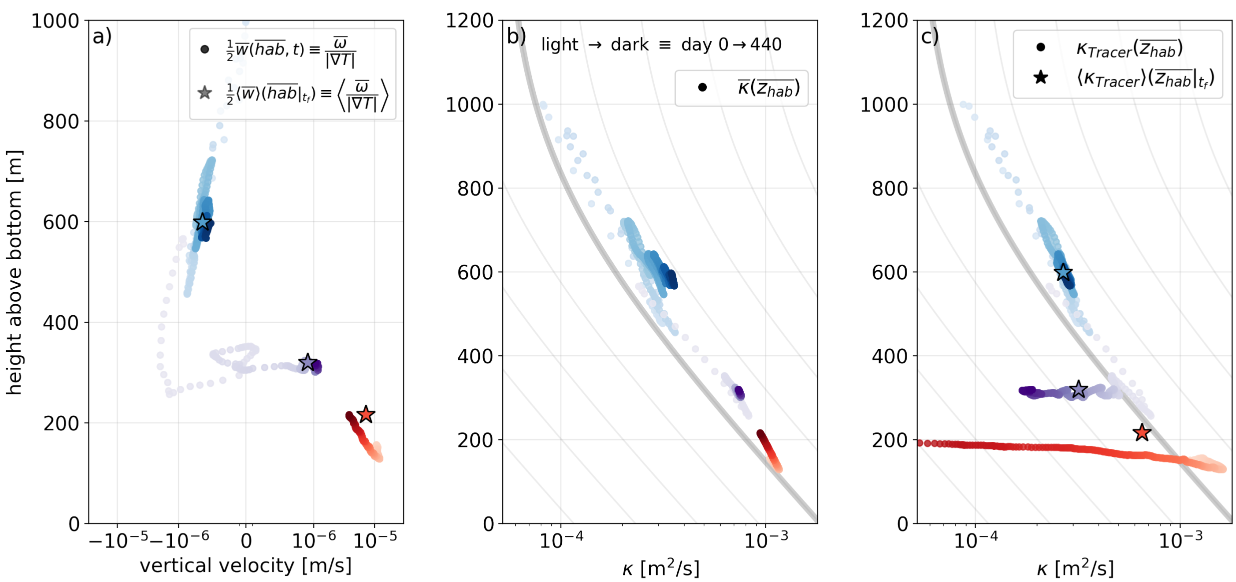

FIG. 7. (a) Height-above-bottom-averaged tracer-weighted buoyancy velocity, normalized by the buoyancy gradient to yield an effective vertical velocity (colors). (b,c) As in (a), but for the tracer-weighted in-situ diffusivity $\overline{\kappa}$ and tracer diffusivity κ_{Tracer}. Dots show trajectories (colors darken over time) in terms of the magnitude of moment tendency terms and the tracer-weighted height-above-bottom ($\overline{\text{hab}}(t)$). Stars in (a,c) show the time-averaged moments, as they would be estimated from a TRE survey 440 days after release (assuming perfect spatial coverage).

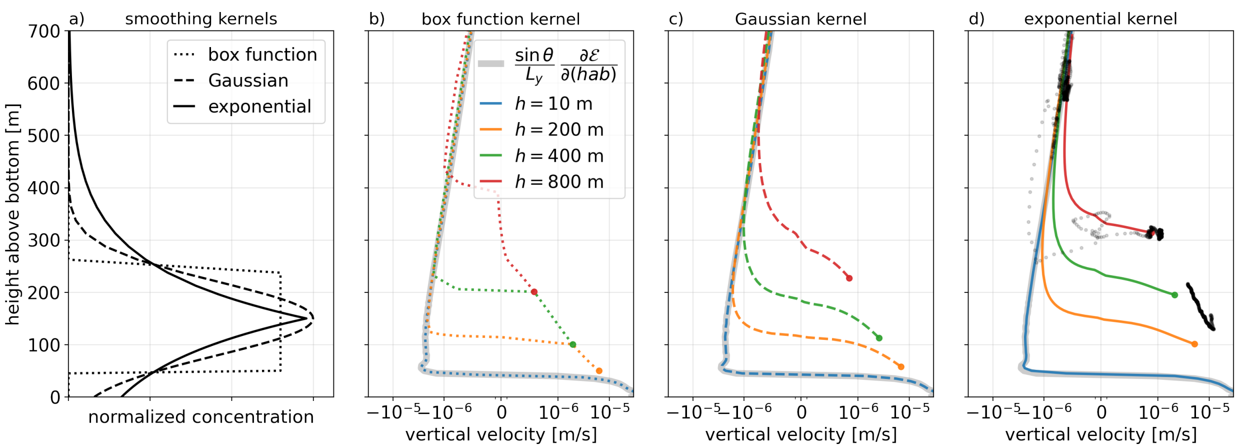

FIG. 8. Understanding the height-above-bottom structure of tracer transport by convolving the average velocity profile with idealized tracer kernels. (a) Three idealized shapes of tracer kernels, shown with a characteristic width of 200 m meters and centered 150 m above the bottom. (b-d) Grey lines show the height-above-bottom averaged effective vertical velocity, estimated using watermass transformation analysis (eq. 11). Colored lines show the result of convolving this profile with idealized kernels (eq. 12) of different shapes (columns) and widths (colors). Black dots in (d) reproduce the snapshots of tracer-weighted buoyancy velocities shown in Figure 7a, for comparison.

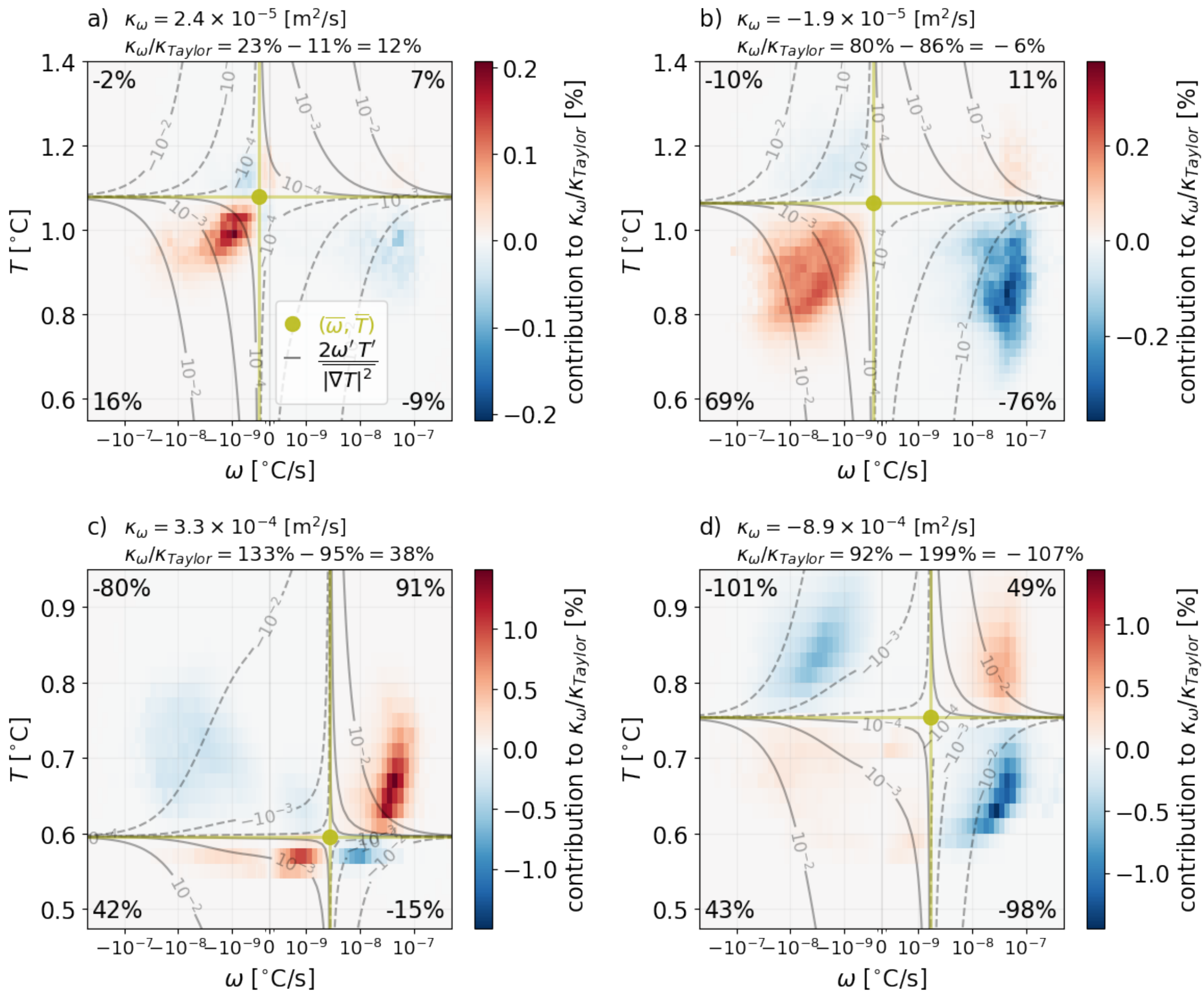

Fig. 9. Percentage contributions to the normalized net diapycnal stretching effect $\kappa_\omega/\kappa_{\text{Taylor}}$ from each (ω, T) bin, as a percentage, for the BBTRE (top) and Bottom (bottom) tracers at 100 days (left) and 440 days (right). The plotted quantity is the summand in eq. 14, which are integrated such that the contributions from each bin (log-spaced in ω) can be visually and quantitatively compared. Numbers in the four corners of each panel show the summed contributions from each of the four quadrants delineated by the respective signs of $\omega' \equiv \omega - \overline{\omega}$ and $T' \equiv T - \overline{T}$. The $\omega' = 0$ and $T' = 0$ lines in olive delineate the four quadrants. For reference, grey contours show the effective diapycnal stretching diffusivity, $\kappa_\omega \equiv 2\frac{\overline{\omega' T'}}{|\nabla T|^2}$, that corresponds to each (ω, T) bin. Subtitles decompose the net diapycnal stretching effect into strictly stretching ($\omega' T' > 0$) and strictly contracting components ($\omega' T' < 0$). PDFs of tracer mass show that a large portion of the tracers' mass does not contribute significantly to these stretching effects (Figure 10).

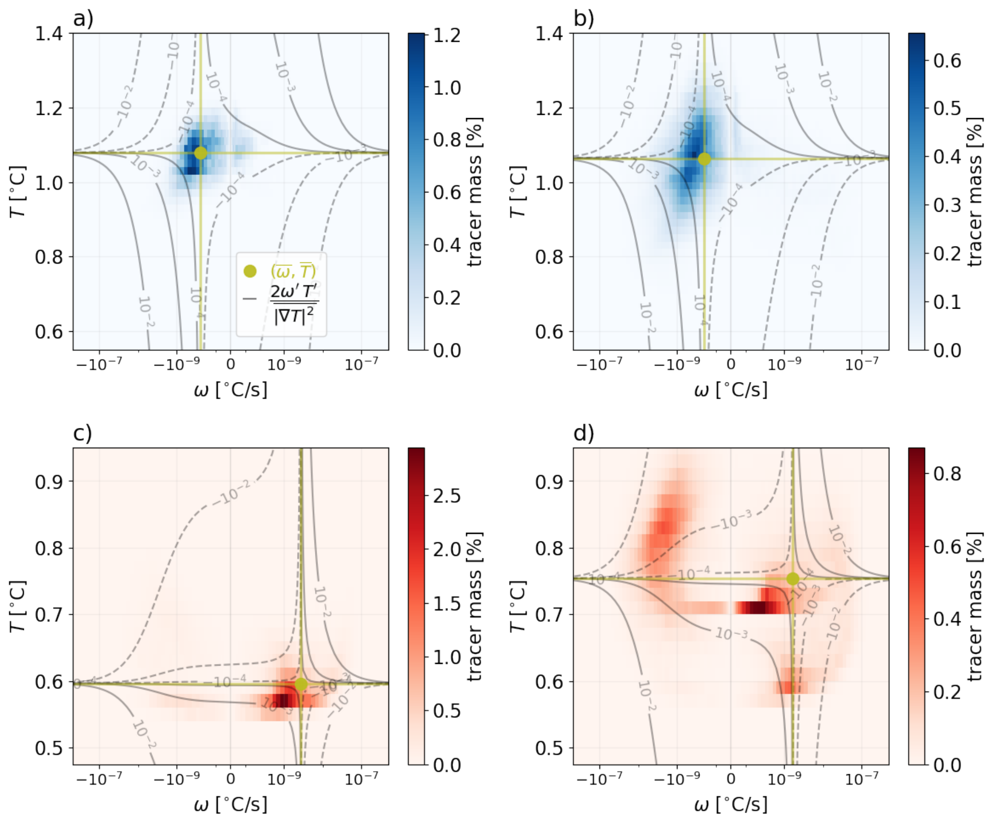

428 Fig. 10. Probability density function of tracer mass, as a percent contribution of each bin to the total tracer
429 mass. Grey contours and olive lines as in Figure 9.

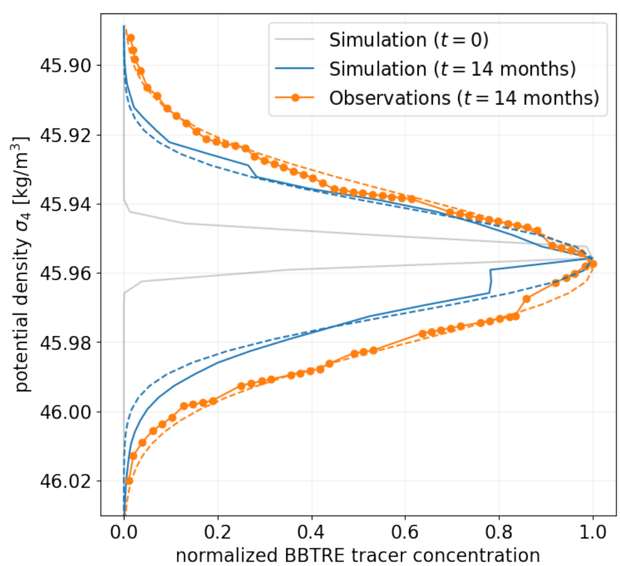

FIG. 11. Simulated and observed tracer distributions in density space at 14 months. We fit a Gaussian distribution $\propto \exp\left\{\frac{-(\sigma_4-\sigma_{4,0})^2}{2\tilde{\kappa}t}\right\}$ to the observations by eye (dashed orange). The simulated distribution is reasonably well fit by a Gaussian distribution corresponding to a diffusivity reduced by a factor of 2 (dashed blue), consistent with the results of the buoyancy moments method (Figure 6c,d).

Acknowledgments. We thank Jim Ledwell for countless insightful discussions about this work and comments on previous versions of the manuscript. We acknowledge funding support from National Science Foundation Awards 6932401 and 6936732. This material is based upon work supported by the National Science Foundation Graduate Research Fellowship Program under Grant No. 174530. Any opinions, findings, and conclusions or recommendations expressed in this material are those of the author(s) and do not necessarily reflect the views of the National Science Foundation.

Data availability statement. The source code for the MITgcm simulations and all of the Python code necessary to produce the figures will be publicly available at `github.com/hdrake/sim-bbtre` upon acceptance (or earlier by requesting the corresponding author). Our analysis of labeled data arrays is greatly simplified by the `xarray` package in Python (Hoyer and Hamman 2017).

APPENDIX A

A slope-native MITgcm configuration of mixing layer flows in the Brazil Basin

We use a hydrostatic formulation of the MIT General Circulation Model (MITgcm; Marshall et al. 1997) to simulate mixing-driven flows in the BBTRE canyon and the transient evolution of three localized tracer releases. Regional bathymetry is extracted from the Global Bathymetry and Topography at 15 Arc Sec dataset (SRTM15+; Tozer et al. 2019) and interpolated onto a locally-tangent Cartesian grid $(\hat{x}, \hat{y}, \hat{z})$ aligned with the BBTRE canyon, where $\hat{x}$ denotes the along-canyon (or cross-ridge) dimension, $\hat{y}$ denotes the cross-canyon (or along-ridge) dimension, and $\hat{d}(\hat{x}, \hat{y})$ is the seafloor depth (Figure 2a). The domain includes both the BBTRE tracer release location and ample room for up-canyon advection of the tracer, which is anticipated based on both the BBTRE observations (Ledwell et al. 2000) and bottom boundary layer theory (Holmes et al. 2019).

Inspired by 1D boundary layer theory and the idealized 3D simulations of Callies (2018), we configure a slope-native implementation of the MITgcm (only summarized here; details in Drake et al., in prep). First, we separate a quiescent ($\mathbf{u}_b \equiv \mathbf{0}$) background with uniform stratification $\Lambda \equiv \frac{\mathrm{d}T_b}{\mathrm{d}\hat{z}} = 9 \times 10^{-4}\,°\mathrm{C/m}$ from the solution and solve only for the perturbations $T_p \equiv T - T_b$ and $\mathbf{u}_p \equiv \mathbf{u} - \mathbf{u}_b$ about this background state, which requires adding the appropriate tendency terms to the perturbation temperature and momentum equations, respectively. Second, we transform the MITgcm into the coordinates of the mean slope, with slope angle $\theta = 1.26 \times 10^{-3}$ (Figure 2b), allowing us to apply periodic boundary conditions to the perturbations in the (x, y) plane of the mean slope. The de-trended seafloor depth is given by $d(x, y) \equiv \hat{d}(\hat{x}, \hat{y}) - \hat{x}\tan\theta$. Mean cross-slope upwelling and downwelling across the periodic **x** boundary provide infinite sources of dense and light waters, respectively, allowing equilibration of the solution without requiring an explicit restoring force to balance the homogenizing tendency of turbulent mixing (Garrett 1991).

A companion paper (Drake et al., in prep.) explores the mixing-driven circulations that arise in this simulation in detail. Bottom-enhanced mixing spins up a broad diapycnal sinking in the well-stratified interior and a vigorous diabatic upwelling in the bottom boundary layer. Despite a modest restratifying effect by this mean overturning circulation, the solution develops a substantial horizontal temperature gradient which stores available potential energy. This available potential energy fuels instabilities, which grow to finite amplitude and are characterized by a Rossby number of $R_o \approx 1$, i.e. are submesoscale in nature (see e.g. McWilliams 2016). One effect of these eddies is to restratify the bottom 20 m or so, bringing the simulated stratification more in line with observations than 1D boundary layer dynamics would suggest (Callies 2018; Ruan and Callies 2020). A hierarchy of progressively simplified versions of the simulation are used as mechanism denial experiments to show the importance of different dynamical processes in controlling the near-bottom stratification, which in turn controls the magnitude of near-bottom diapycnal upwelling.

In our slope-native configuration, one should imagine infinitely many copies of TREs, each separated by a horizontal distance $L_x = 480\,\text{km}$ (domain length) and vertical height $L_x \tan\theta \approx 1000\,\text{m}$ (corresponding to a background temperature difference $\Delta T \approx \frac{\mathrm{d}T_b}{\mathrm{d}\hat{z}} L_x \sin\theta = 0.52\,°\text{C}$). A limitation of this configuration is that by 1000 days enough of the tracer crosses the periodic boundaries that the copies of the tracers begin significantly interfering with each other and the temperature moment calculations become meaningless, which is why we truncate the simulations after the timing of the first BBTRE survey (14 months $\approx$ 440 days). For all of the analysis presented here, we re-center our periodic domain on the center of mass of a single copy of the tracer cloud before adding the background state (i.e. the constantly stratified background temperature field T_b) back in and then we crop the infinite domain to ignore other copies of the tracer (similar to the approach used to compute watermass transformations in Appendix B).

APPENDIX B

Eulerian and tracer-weighted watermass transformations

A natural framework for understanding the drivers of diapycnal transport is watermass transformation analysis (Walin 1982; Marshall et al. 1999), which reframes the buoyancy budget in buoyancy space by integrating along buoyancy surfaces (or over buoyancy classes). Following Ferrari et al. (2016), the diapycnal transport $\mathcal{E}(T,t)$ across a buoyancy surface $\mathcal{A}(T)$ is given by

$$\mathcal{E}(T,t) \equiv \iint_{\mathcal{A}(T)} \mathbf{e}\cdot\mathbf{n}\,\mathrm{d}A = \partial_T \int_{\mathcal{V}(\tilde{T}<T)} \omega\,\mathrm{d}V, \tag{B1}$$

where $\mathbf{e} \equiv \left(\mathbf{u}\cdot\mathbf{n} - \frac{T_t}{|\nabla T|}\right)\mathbf{n}$ is the diapycnal velocity and $\mathcal{V}(\tilde{T} < T)$ is the volume enclosing any water denser than T. Since our simulations have not fully equilibrated in the SML, diapycnal transports include two components: flow across a buoyancy surface and the movement of the buoyancy surfaces themselves. In the present context, it is useful to distinguish contributions to the diapycnal transport from a strictly upwelling BBL component, where the integral is only evaluated over the strictly upwelling volume $\mathcal{V}(\tilde{T} < T; \omega > 0)$, and a strictly downwelling SML component, similarly defined (see Figure B1).

In practice, meaningful evaluation of this integral in the slope-native configuration requires stitching together $H/(L_x \tan\theta) \approx \mathcal{O}(5)$ periodic copies of the domain (where H is the height of the domain) before adding in the background buoyancy field B, so that each isopycnal can be followed all the way from its incrop at the seafloor to the interior far-field where mixing is weak (Figure B1). Further, because our simulation is periodic in the cross-slope direction (and thus in mean buoyancy), the resulting watermass transformations are periodic over a buoyancy interval $\Delta T = \Lambda L_x \tan\theta \approx 0.52\,^\circ$C. Temporal variability of watermass transformations is small relative to the other variations we focus on, so all results hereafter refer to their time-mean.

Averaging over a buoyancy layer of thickness ΔT yields a single representative value of the net watermass transformation,

$$\overline{\mathcal{E}}^T \equiv \frac{1}{\Delta T}\int_T^{T+\Delta T} \mathcal{E}(\tilde{T})\,\mathrm{d}\tilde{T} = \int_{\mathcal{V}(T<\tilde{T}<T+\Delta T)} \frac{\omega}{\Delta T}\,\mathrm{d}V. \tag{B2}$$

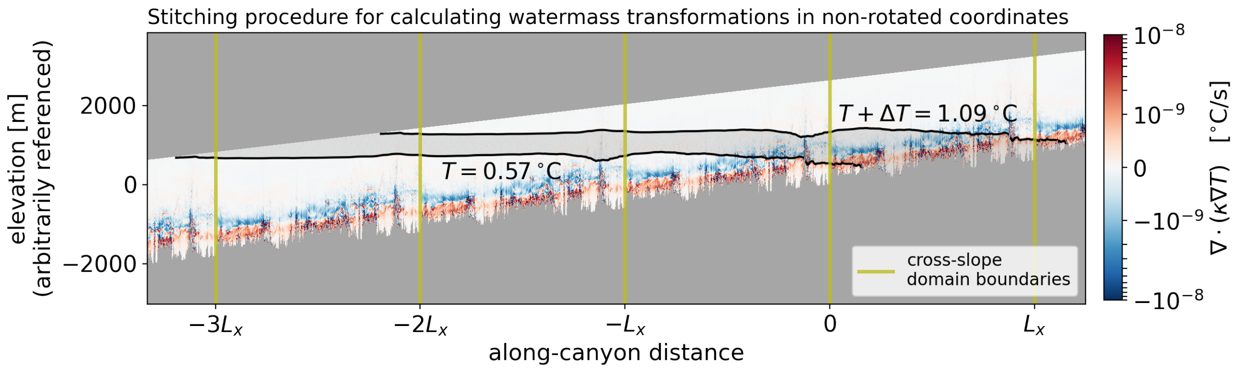

FIG. B1. Turbulent buoyancy (temperature) flux convergence along the trough of the BBTRE canyon. Vertical olive lines show along-canyon boundaries of the simulation domain; the solution is doubly periodic in buoyancy perturbations, but discontinuous in the total buoyancy in the along-canyon direction due to a constant background mean slope and stratification. For the small mean slopes considered here, computing watermass transformations thus requires reconstructing the full extent of buoyancy surfaces by stitching together multiple copies of the domain, each translated by a multiple of the domain extent L_x and by a background temperature jump $\Delta T = \Lambda \Delta z \approx 0.52\,^{\circ}\mathrm{C}$ (where $\Delta z = L_x \tan\theta$ is the layer thickness).

This equation is also reminiscent of that for the evolution of the first tracer-weighted buoyancy moment (3), with the whole domain being weighted equally as opposed to being weighted by the tracer concentration.

The detailed height-above-bottom (η, for short) structure of upwelling and downwelling watermass transformations are also of interest, since these are more directly comparable with measurements from vertical profilers, 1D BBL theory, and the diapycnal transport of localized tracers. Building upon Holmes and McDougall (2020), we define the height-above-bottom cumulative watermass transformation as:

$$\overline{\mathcal{E}}^{T}(\eta) = \int_{\mathcal{V}(T_0 < \tilde{T} < T_0 + \Delta T;\, \tilde{\eta} < \eta)} \frac{\omega}{\Delta T}\, \mathrm{d}V. \tag{B3}$$

We aim to convert these watermass transformations into effective vertical velocities, for more direct comparison with the tracer diagnostics. Loosely, taking the slope-normal (or η) derivative provides the up-slope upwelling flux (in m^2/s) at a given height-above-bottom:

$$\frac{\partial}{\partial \eta}\overline{\mathcal{E}}^{T}(\eta) = \frac{\partial}{\partial \eta}\int_{\mathcal{V}(T_0<\tilde{T}<T_0+\Delta T;\, \tilde{\eta}<\eta)} \frac{\omega}{\Delta T}\,\mathrm{d}V. \tag{B4}$$

Multiplying by $\sin\theta$ approximately converts this to a vertical flux, and dividing by the width L_y of the domain finishes the conversion to the effective velocity (11). Profiles of $\overline{W}^{T}(\eta)$ are shown in Figure 8 and, after convolution with idealized height-above-bottom tracer distributions, compare favorably with the diagnosed vertical structure of tracer upwelling.

References

Abernathey, R. P., I. Cerovecki, P. R. Holland, E. Newsom, M. Mazloff, and L. D. Talley, 2016: Water-mass transformation by sea ice in the upper branch of the Southern Ocean overturning. *Nature Geoscience*, **9 (8)**, 596–601, https://doi.org/10.1038/ngeo2749, URL http://www.nature.com/articles/ngeo2749, publisher: Nature Publishing Group.

Alberty, M. S., S. Billheimer, M. M. Hamann, C. Y. Ou, V. Tamsitt, A. J. Lucas, and M. H. Alford, 2017: A reflecting, steepening, and breaking internal tide in a submarine canyon. *Journal of Geophysical Research: Oceans*, **122 (8)**, 6872–6882, https://doi.org/10.1002/2016JC012583, URL https://onlinelibrary.wiley.com/doi/abs/10.1002/2016JC012583, _eprint: https://onlinelibrary.wiley.com/doi/pdf/10.1002/2016JC012583.

Baker, M. A., and C. H. Gibson, 1987: Sampling Turbulence in the Stratified Ocean: Statistical Consequences of Strong Intermittency. *Journal of Physical Oceanography*, **17 (10)**, 1817–1836, https://doi.org/10.1175/1520-0485(1987)017<1817:STITSO>2.0.CO;2, URL https://journals.ametsoc.org/view/journals/phoc/17/10/1520-0485_1987_017_1817_stitso_2_0_co_2.xml, publisher: American Meteorological Society Section: Journal of Physical Oceanography.

Bryan, K., and L. J. Lewis, 1979: A water mass model of the world ocean. *Journal of Geophysical Research*, **84 (C5)**, 2503–2517, https://doi.org/10.1029/JC084iC05p02503, iSBN: 0148-0227.

Cael, B., and A. Mashayek, 2021: Log-Skew-Normality of Ocean Turbulence. *Physical Review Letters*, **126 (22)**, 224 502, https://doi.org/10.1103/PhysRevLett.126.224502, URL https://link.

aps.org/doi/10.1103/PhysRevLett.126.224502, publisher: American Physical Society.

Callies, J., 2018: Restratification of Abyssal Mixing Layers by Submesoscale Baroclinic Eddies. *Journal of Physical Oceanography*, JPO–D–18–0082.1, https://doi.org/10.1175/JPO-D-18-0082.1, URL http://journals.ametsoc.org/doi/10.1175/JPO-D-18-0082.1.

Callies, J., and R. Ferrari, 2018: Dynamics of an Abyssal Circulation Driven by Bottom-Intensified Mixing on Slopes. *Journal of Physical Oceanography*, **48 (6)**, 1257–1282, https://doi.org/10.1175/JPO-D-17-0125.1, URL http://journals.ametsoc.org/doi/10.1175/JPO-D-17-0125.1.

Clément, L., A. M. Thurnherr, and L. C. St. Laurent, 2017: Turbulent Mixing in a Deep Fracture Zone on the Mid-Atlantic Ridge. *Journal of Physical Oceanography*, **47 (8)**, 1873–1896, https://doi.org/10.1175/JPO-D-16-0264.1, URL http://journals.ametsoc.org/doi/10.1175/JPO-D-16-0264.1.

de Lavergne, C., G. Madec, J. Le Sommer, A. J. G. Nurser, and A. C. Naveira Garabato, 2016a: The Impact of a Variable Mixing Efficiency on the Abyssal Overturning. *Journal of Physical Oceanography*, **46 (2)**, 663–681, https://doi.org/10.1175/JPO-D-14-0259.1, URL http://journals.ametsoc.org/doi/10.1175/JPO-D-14-0259.1.

de Lavergne, C., G. Madec, J. Le Sommer, A. J. G. Nurser, and A. C. Naveira Garabato, 2016b: On the Consumption of Antarctic Bottom Water in the Abyssal Ocean. *Journal of Physical Oceanography*, **46 (2)**, 635–661, https://doi.org/10.1175/JPO-D-14-0201.1, URL http://journals.ametsoc.org/doi/10.1175/JPO-D-14-0201.1.

de Lavergne, C., and Coauthors, 2020: A Parameterization of Local and Remote Tidal Mixing. *Journal of Advances in Modeling Earth Systems*, **12 (5)**, e2020MS002 065, https://doi.org/https://doi.org/10.1029/2020MS002065, URL https://agupubs.onlinelibrary.wiley.com/doi/abs/10.1029/2020MS002065, _eprint: https://agupubs.onlinelibrary.wiley.com/doi/pdf/10.1029/2020MS002065.

Dillon, T. M., 1982: Vertical overturns: A comparison of Thorpe and Ozmidov length scales. *Journal of Geophysical Research: Oceans*, **87 (C12)**, 9601–9613, https://doi.org/https://doi.org/10.1029/JC087iC12p09601, URL https:

//agupubs.onlinelibrary.wiley.com/doi/abs/10.1029/JC087iC12p09601, _eprint: https://agupubs.onlinelibrary.wiley.com/doi/pdf/10.1029/JC087iC12p09601.

Drake, H. F., R. Ferrari, and J. Callies, 2020: Abyssal Circulation Driven by Near-Boundary Mixing: Water Mass Transformations and Interior Stratification. *Journal of Physical Oceanography*, **50 (8)**, 2203–2226, https://doi.org/10.1175/JPO-D-19-0313.1, URL https://journals.ametsoc.org/jpo/article/50/8/2203/348530/Abyssal-Circulation-Driven-by-Near-Boundary-Mixing, publisher: American Meteorological Society.

Ferrari, R., A. Mashayek, T. J. McDougall, M. Nikurashin, and J.-M. Campin, 2016: Turning Ocean Mixing Upside Down. *Journal of Physical Oceanography*, **46 (7)**, 2239–2261, https://doi.org/10.1175/JPO-D-15-0244.1, URL http://journals.ametsoc.org/doi/10.1175/JPO-D-15-0244.1.

Garrett, C., 1991: Marginal mixing theories. *Atmosphere-Ocean*, **29 (2)**, 313–339, https://doi.org/10.1080/07055900.1991.9649407, URL http://www.tandfonline.com/doi/abs/10.1080/07055900.1991.9649407.

Garrett, C., P. MacCready, and P. Rhines, 1993: Boundary Mixing and Arrested Ekman Layers: Rotating Stratified Flow Near a Sloping Boundary. *Annual Review of Fluid Mechanics*, **25 (1)**, 291–323, https://doi.org/10.1146/annurev.fl.25.010193.001451, URL http://www.annualreviews.org/doi/10.1146/annurev.fl.25.010193.001451, publisher: Annual Reviews 4139 El Camino Way, P.O. Box 10139, Palo Alto, CA 94303-0139, USA.

Garrett, C., and W. Munk, 1972: Space-Time scales of internal waves. *Geophysical Fluid Dynamics*, **3 (3)**, 225–264, https://doi.org/10.1080/03091927208236082, URL https://doi.org/10.1080/03091927208236082, publisher: Taylor & Francis _eprint: https://doi.org/10.1080/03091927208236082.

Garrett, C., and W. Munk, 1975: Space-time scales of internal waves: A progress report. *Journal of Geophysical Research (1896-1977)*, **80 (3)**, 291–297, https://doi.org/10.1029/JC080i003p00291, URL https://agupubs.onlinelibrary.wiley.com/doi/abs/10.1029/JC080i003p00291, _eprint: https://agupubs.onlinelibrary.wiley.com/doi/pdf/10.1029/JC080i003p00291.

Gregg, M., E. D'Asaro, J. Riley, and E. Kunze, 2018: Mixing Efficiency in the Ocean. *Annual Review of Marine Science*, **10 (1)**, 443–473, https://doi.org/10.1146/annurev-marine-121916-063643, URL http://www.annualreviews.org/doi/10.1146/annurev-marine-121916-063643.

Gregg, M. C., 1989: Scaling turbulent dissipation in the thermocline. *Journal of Geophysical Research*, **94 (C7)**, 9686, https://doi.org/10.1029/JC094iC07p09686, URL http://doi.wiley.com/10.1029/JC094iC07p09686.

Gregg, M. C., T. B. Sanford, and D. P. Winkel, 2003: Reduced mixing from the breaking of internal waves in equatorial waters. *Nature*, **422 (6931)**, 513–515, https://doi.org/10.1038/nature01507, URL https://www.nature.com/articles/nature01507, number: 6931 Publisher: Nature Publishing Group.

Hamann, M. M., M. H. Alford, A. J. Lucas, A. F. Waterhouse, and G. Voet, 2021: Turbulence Driven by Reflected Internal Tides in a Supercritical Submarine Canyon. *Journal of Physical Oceanography*, **51 (2)**, 591–609, https://doi.org/10.1175/JPO-D-20-0123.1, URL https://journals.ametsoc.org/view/journals/phoc/51/2/jpo-d-20-0123.1.xml, publisher: American Meteorological Society Section: Journal of Physical Oceanography.

Henyey, F. S., J. Wright, and S. M. Flatté, 1986: Energy and action flow through the internal wave field: An eikonal approach. *Journal of Geophysical Research: Oceans*, **91 (C7)**, 8487–8495, https://doi.org/10.1029/JC091iC07p08487, URL https://agupubs.onlinelibrary.wiley.com/doi/abs/10.1029/JC091iC07p08487, _eprint: https://agupubs.onlinelibrary.wiley.com/doi/pdf/10.1029/JC091iC07p08487.

Hogg, N., P. Biscaye, W. Gardner, and W. Jr, 1982: On the Transport and Modification of Antarctic Bottom Water in the Vema Channel. *J. Mar. Res.*, **40**, 231–263.

Holmes, R. M., C. de Lavergne, and T. J. McDougall, 2019: Tracer Transport within Abyssal Mixing Layers. *Journal of Physical Oceanography*, **49 (10)**, 2669–2695, https://doi.org/10.1175/JPO-D-19-0006.1, URL https://journals.ametsoc.org/doi/full/10.1175/JPO-D-19-0006.1, publisher: American Meteorological Society.

Holmes, R. M., and T. J. McDougall, 2020: Diapycnal Transport near a Sloping Bottom Boundary. *Journal of Physical Oceanography*, **50 (11)**, 3253–3266, https://doi.org/10.1175/JPO-D-20-0066.1, URL https://journals.ametsoc.org/view/journals/phoc/50/11/jpoD200066.xml, publisher: American Meteorological Society Section: Journal of Physical Oceanography.

Holtermann, P. L., L. Umlauf, T. Tanhua, O. Schmale, G. Rehder, and J. J. Waniek, 2012: The Baltic Sea Tracer Release Experiment: 1. Mixing rates. *Journal of Geophysical Research: Oceans*, **117 (C1)**, https://doi.org/10.1029/2011JC007439, URL https://onlinelibrary.wiley.com/doi/abs/10.1029/2011JC007439, _eprint: https://onlinelibrary.wiley.com/doi/pdf/10.1029/2011JC007439.

Hoyer, S., and J. Hamman, 2017: xarray: N-D labeled arrays and datasets in Python. *Journal of Open Research Software*, **5 (1)**, https://doi.org/10.5334/jors.148, URL http://doi.org/10.5334/jors.148.

Huang, R. X., and X. Jin, 2002: Deep Circulation in the South Atlantic Induced by Bottom-Intensified Mixing over the Midocean Ridge*. *Journal of Physical Oceanography*, **32 (4)**, 1150–1164, https://doi.org/10.1175/1520-0485(2002)032<1150:DCITSA>2.0.CO;2.

Kunze, E., E. Firing, J. M. Hummon, T. K. Chereskin, and A. M. Thurnherr, 2006: Global Abyssal Mixing Inferred from Lowered ADCP Shear and CTD Strain Profiles. *Journal of Physical Oceanography*, **36 (8)**, 1553–1576, https://doi.org/10.1175/JPO2926.1, URL https://journals.ametsoc.org/view/journals/phoc/36/8/jpo2926.1.xml, publisher: American Meteorological Society Section: Journal of Physical Oceanography.

Ledwell, J. R., T. F. Duda, M. A. Sundermeyer, and H. E. Seim, 2004: Mixing in a coastal environment: 1. A view from dye dispersion. *Journal of Geophysical Research: Oceans*, **109 (C10)**, https://doi.org/https://doi.org/10.1029/2003JC002194, URL https://agupubs.onlinelibrary.wiley.com/doi/abs/10.1029/2003JC002194, _eprint: https://agupubs.onlinelibrary.wiley.com/doi/pdf/10.1029/2003JC002194.

Ledwell, J. R., R. He, Z. Xue, S. F. DiMarco, L. J. Spencer, and P. Chapman, 2016: Dispersion of a tracer in the deep Gulf of Mexico. *Journal of Geophysical Research: Oceans*, **121 (2)**, 1110–1132, https://doi.org/https://doi.org/10.1002/

2015JC011405, URL https://agupubs.onlinelibrary.wiley.com/doi/abs/10.1002/2015JC011405, _eprint: https://agupubs.onlinelibrary.wiley.com/doi/pdf/10.1002/2015JC011405.

Ledwell, J. R., and B. M. Hickey, 1995: Evidence for enhanced boundary mixing in the Santa Monica Basin. *Journal of Geophysical Research: Oceans*, **100 (C10)**, 20 665–20 679, https://doi.org/https://doi.org/10.1029/94JC01182, URL https://agupubs.onlinelibrary.wiley.com/doi/abs/10.1029/94JC01182, _eprint: https://agupubs.onlinelibrary.wiley.com/doi/pdf/10.1029/94JC01182.

Ledwell, J. R., E. T. Montgomery, K. L. Polzin, L. C. St. Laurent, R. W. Schmitt, and J. M. Toole, 2000: Evidence for enhanced mixing over rough topography in the abyssal ocean. *Nature*, **403 (6766)**, 179–182, https://doi.org/10.1038/35003164, URL http://www.nature.com/articles/35003164, publisher: Nature Publishing Group.

Ledwell, J. R., A. J. Watson, and C. S. Law, 1998: Mixing of a tracer in the pycnocline. *Journal of Geophysical Research: Oceans*, **103 (C10)**, 21 499–21 529, https://doi.org/https://doi.org/10.1029/98JC01738, URL https://agupubs.onlinelibrary.wiley.com/doi/abs/10.1029/98JC01738, _eprint: https://agupubs.onlinelibrary.wiley.com/doi/pdf/10.1029/98JC01738.

Lele, R., and Coauthors, 2021: Abyssal Heat Budget in the Southwest Pacific Basin. *Journal of Physical Oceanography*, **51 (11)**, 3317–3333, https://doi.org/10.1175/JPO-D-21-0045.1, URL https://journals.ametsoc.org/view/journals/phoc/51/11/JPO-D-21-0045.1.xml, publisher: American Meteorological Society Section: Journal of Physical Oceanography.

Lumpkin, R., and K. Speer, 2007: Global Ocean Meridional Overturning. *Journal of Physical Oceanography*, **37 (10)**, 2550–2562, https://doi.org/10.1175/JPO3130.1, URL http://dx.doi.org/10.1175/JPO3130.1, iSBN: 0022-3670.

Mackay, N., J. R. Ledwell, M.-J. Messias, A. C. N. Garabato, J. A. Brearley, A. J. S. Meijers, D. C. Jones, and A. J. Watson, 2018: Diapycnal Mixing in the Southern Ocean Diagnosed Using the DIMES Tracer and Realistic Velocity Fields. *Journal of Geophysical Research: Oceans*, **123 (4)**, 2615–2634, https://doi.org/https://doi.org/10.1002/2017JC013536, URL https://agupubs.onlinelibrary.wiley.com/doi/abs/10.1002/2017JC013536, _eprint: https://agupubs.onlinelibrary.wiley.com/doi/pdf/10.1002/2017JC013536.

MacKinnon, J. A., and Coauthors, 2017: Climate Process Team on Internal Wave–Driven Ocean Mixing. *Bulletin of the American Meteorological Society*, **98 (11)**, 2429–2454, https://doi.org/10.1175/BAMS-D-16-0030.1, URL http://journals.ametsoc.org/doi/10.1175/BAMS-D-16-0030.1.

Marshall, J., C. Hill, L. Perelman, and A. Adcroft, 1997: Hydrostatic, quasi-hydrostatic, and non-hydrostatic ocean modeling. *Journal of Geophysical Research*, **102 (C3)**, 5733, https://doi.org/10.1029/96JC02776, iSBN: 2156-2202.

Marshall, J., D. Jamous, and J. Nilsson, 1999: Reconciling thermodynamic and dynamic methods of computation of water-mass transformation rates. *Deep-Sea Research Part I: Oceanographic Research Papers*, **46 (4)**, 545–572, https://doi.org/10.1016/S0967-0637(98)00082-X, iSBN: 0967-0637.

Mashayek, A., R. Ferrari, S. Merrifield, J. R. Ledwell, L. St Laurent, and A. N. Garabato, 2017: Topographic enhancement of vertical turbulent mixing in the Southern Ocean. *Nature Communications*, **8**, 14 197, https://doi.org/10.1038/ncomms14197, URL http://www.nature.com/doifinder/10.1038/ncomms14197, publisher: Nature Publishing Group.

McDougall, T. J., and R. Ferrari, 2017: Abyssal Upwelling and Downwelling Driven by Near-Boundary Mixing. *Journal of Physical Oceanography*, **47 (2)**, 261–283, https://doi.org/10.1175/JPO-D-16-0082.1, URL https://journals.ametsoc.org/doi/full/10.1175/JPO-D-16-0082.1, publisher: American Meteorological Society.

McWilliams, J. C., 2016: Submesoscale currents in the ocean. *Proceedings of the Royal Society A: Mathematical, Physical and Engineering Sciences*, **472 (2189)**, 20160 117, https://doi.org/10.1098/rspa.2016.0117, URL https://royalsocietypublishing.org/doi/10.1098/rspa.2016.0117, publisher: Royal Society.

Munk, W. H., 1966: Abyssal recipes. *Deep Sea Research and Oceanographic Abstracts*, **13 (4)**, 707–730, https://doi.org/10.1016/0011-7471(66)90602-4, arXiv: cs/9605103 ISBN: 1600117471.

Munk, W. H., and C. Wunsch, 1998: Abyssal Recipes II: energetics of tidal and wind mixing. *Deep-Sea Research Part I: Oceanographic Research Papers*, **45**, 1978–2010.

Nazarian, R. H., C. M. Burns, S. Legg, M. C. Buijsman, H. Kaur, and B. K. Arbic, 2021: On the Magnitude of Canyon-Induced Mixing. *Journal of Geophysical Research: Oceans*, **126 (11)**, e2021JC017 671, https://doi.org/10.1029/2021JC017671, URL https://onlinelibrary.wiley.com/doi/abs/10.1029/2021JC017671, _eprint: https://onlinelibrary.wiley.com/doi/pdf/10.1029/2021JC017671.

Nikurashin, M., and R. Ferrari, 2009: Radiation and Dissipation of Internal Waves Generated by Geostrophic Motions Impinging on Small-Scale Topography: Theory. *Journal of Physical Oceanography*, **40 (5)**, 1055–1074, https://doi.org/10.1175/2009JPO4199.1, URL https://journals.ametsoc.org/doi/full/10.1175/2009JPO4199.1.

Nikurashin, M., and S. Legg, 2011: A Mechanism for Local Dissipation of Internal Tides Generated at Rough Topography. *Journal of Physical Oceanography*, **41 (2)**, 378–395, https://doi.org/10.1175/2010JPO4522.1, URL http://journals.ametsoc.org/doi/abs/10.1175/2010JPO4522.1.

Osborn, T. R., 1980: Estimates of the Local Rate of Vertical Diffusion from Dissipation Measurements. *Journal of Physical Oceanography*, **10 (1)**, 83–89, https://doi.org/10.1175/1520-0485(1980)010<0083:EOTLRO>2.0.CO;2, URL http://journals.ametsoc.org/doi/abs/10.1175/1520-0485%281980%29010%3C0083%3AEOTLRO%3E2.0.CO%3B2.

Osborn, T. R., and C. S. Cox, 1972: Oceanic fine structure. *Geophysical Fluid Dynamics*, **3 (1)**, 321–345, https://doi.org/10.1080/03091927208236085, URL http://www.tandfonline.com/doi/abs/10.1080/03091927208236085.

Polzin, K., J. Toole, J. R. Ledwell, and R. Schmitt, 1997: Spatial Variability of Turbulent Mixing in the Spatial Variability Abyssal Ocean. *Science*, **276 (5309)**, 93–96, https://doi.org/10.1126/science.276.5309.93, URL http://www.sciencemag.org/cgi/content/abstract/276/5309/93, iSBN: 0036-8075.

Polzin, K. L., 2009: An abyssal recipe. *Ocean Modelling*, **30 (4)**, 298–309, https://doi.org/10.1016/j.ocemod.2009.07.006.

Polzin, K. L., and T. J. McDougall, 2022: Chapter 7 - Mixing at the ocean's bottom boundary. *Ocean Mixing*, M. Meredith, and A. Naveira Garabato, Eds., Elsevier, 145–180, https://doi.org/

10.1016/B978-0-12-821512-8.00014-1, URL https://www.sciencedirect.com/science/article/pii/B9780128215128000141.

Polzin, K. L., J. M. Toole, R. W. Schmitt, K. L. Polzin, J. M. Toole, and R. W. Schmitt, 1995: Finescale Parameterizations of Turbulent Dissipation. *Journal of Physical Oceanography*, **25 (3)**, 306–328, https://doi.org/10.1175/1520-0485(1995)025<0306:FPOTD>2.0.CO;2.

Ruan, X., and J. Callies, 2020: Mixing-Driven Mean Flows and Submesoscale Eddies over Mid-Ocean Ridge Flanks and Fracture Zone Canyons. *Journal of Physical Oceanography*, **50 (1)**, 175–195, https://doi.org/10.1175/JPO-D-19-0174.1, URL https://journals.ametsoc.org/view/journals/phoc/50/1/jpo-d-19-0174.1.xml, publisher: American Meteorological Society Section: Journal of Physical Oceanography.

Ruan, X., and R. Ferrari, 2021: Diagnosing Diapycnal Mixing from Passive Tracers. *Journal of Physical Oceanography*, **51 (3)**, 757–767, https://doi.org/10.1175/JPO-D-20-0194.1, URL https://journals.ametsoc.org/view/journals/phoc/51/3/JPO-D-20-0194.1.xml, publisher: American Meteorological Society Section: Journal of Physical Oceanography.

Simmons, H. L., S. R. Jayne, L. C. St. Laurent, and A. J. Weaver, 2004: Tidally driven mixing in a numerical model of the ocean general circulation. *Ocean Modelling*, **6 (3-4)**, 245–263, https://doi.org/10.1016/S1463-5003(03)00011-8, iSBN: 1463-5003.

Spingys, C. P., A. C. N. Garabato, S. Legg, K. L. Polzin, E. P. Abrahamsen, C. E. Buckingham, A. Forryan, and E. E. Frajka-Williams, 2021: Mixing and Transformation in a Deep Western Boundary Current: A Case Study. *Journal of Physical Oceanography*, **51 (4)**, 1205–1222, https://doi.org/10.1175/JPO-D-20-0132.1, URL https://journals.ametsoc.org/view/journals/phoc/aop/JPO-D-20-0132.1/JPO-D-20-0132.1.xml, publisher: American Meteorological Society Section: Journal of Physical Oceanography.

St. Laurent, L., and R. W. Schmitt, 1999: The Contribution of Salt Fingers to Vertical Mixing in the North Atlantic Tracer Release Experiment. *Journal of Physical Oceanography*, **29 (7)**, 1404–1424, https://doi.org/10.1175/1520-0485(1999)029<1404:TCOSFT>2.0.CO;2, URL https://journals.ametsoc.org/view/journals/phoc/29/7/1520-0485_1999_029_1404_tcosft_2.0.co_2.xml, publisher: American Meteorological Society Section: Journal of Physical Oceanography.

St. Laurent, L. C., J. M. Toole, and R. W. Schmitt, 2001: Buoyancy Forcing by Turbulence above Rough Topography in the Abyssal Brazil Basin*. *Journal of Physical Oceanography*, **31 (12)**, 3476–3495, https://doi.org/10.1175/1520-0485(2001)031<3476:BFBTAR>2.0.CO;2.

Stommel, H., and A. B. Arons, 1959: On the abyssal circulation of the world ocean — II. An idealized model of the circulation pattern and amplitude in oceanic basins. *Deep Sea Research (1953)*, **6**, 217–233, https://doi.org/10.1016/0146-6313(59)90075-9, URL http://www.sciencedirect.com/science/article/pii/0146631359900759.

Sundermeyer, M. A., E. A. Terray, J. R. Ledwell, A. G. Cunningham, P. E. LaRocque, J. Banic, and W. J. Lillycrop, 2007: Three-Dimensional Mapping of Fluorescent Dye Using a Scanning, Depth-Resolving Airborne Lidar. *Journal of Atmospheric and Oceanic Technology*, **24 (6)**, 1050–1065, https://doi.org/10.1175/JTECH2027.1, URL https://journals.ametsoc.org/view/journals/atot/24/6/jtech2027_1.xml, publisher: American Meteorological Society Section: Journal of Atmospheric and Oceanic Technology.

Talley, L. D., 2013: Closure of the Global Overturning Circulation Through the Indian, Pacific, and Southern Oceans: Schematics and Transports. *Oceanography*, **26 (1)**, 80–97, https://doi.org/10.5670/oceanog.2013.07, URL http://apps.webofknowledge.com/full_record.do?product=UA&search_mode=GeneralSearch&qid=14&SID=W1jPgx8kkS6brME6NvD&page=1&doc=1, arXiv: 1011.1669v3 ISBN: 1042-8275.

Taylor, G. I., 1922: Diffusion by Continuous Movements. *Proceedings of the London Mathematical Society*, **s2-20 (1)**, 196–212, https://doi.org/https://doi.org/10.1112/plms/s2-20.1.196, URL https://londmathsoc.onlinelibrary.wiley.com/doi/abs/10.1112/plms/s2-20.1.196, _eprint: https://londmathsoc.onlinelibrary.wiley.com/doi/pdf/10.1112/plms/s2-20.1.196.

Thorpe, S. A., and G. E. R. Deacon, 1977: Turbulence and mixing in a Scottish Loch. *Philosophical Transactions of the Royal Society of London. Series A, Mathematical and Physical Sciences*, **286 (1334)**, 125–181, https://doi.org/10.1098/rsta.1977.0112, URL https://royalsocietypublishing.org/doi/10.1098/rsta.1977.0112, publisher: Royal Society.

Thurnherr, A. M., L. Clément, L. S. Laurent, R. Ferrari, and T. Ijichi, 2020: Transformation and Upwelling of Bottom Water in Fracture Zone Valleys. *Journal of Physical Oceanography*, **50 (3)**, 715–726, https://doi.org/10.1175/JPO-D-19-0021.1, URL https://journals.ametsoc.

org/view/journals/phoc/50/3/jpo-d-19-0021.1.xml, publisher: American Meteorological Society Section: Journal of Physical Oceanography.

Thurnherr, A. M., and Coauthors, 2005: Mixing Associated with Sills in a Canyon on the Midocean Ridge Flank*. *Journal of Physical Oceanography*, **35 (8)**, 1370–1381, https://doi.org/10.1175/JPO2773.1, URL http://journals.ametsoc.org/doi/abs/10.1175/JPO2773.1.

Tozer, B., D. T. Sandwell, W. H. F. Smith, C. Olson, J. R. Beale, and P. Wessel, 2019: Global Bathymetry and Topography at 15 Arc Sec: SRTM15+. *Earth and Space Science*, **6 (10)**, 1847–1864, https://doi.org/10.1029/2019EA000658, URL https://agupubs.onlinelibrary.wiley.com/doi/abs/10.1029/2019EA000658, _eprint: https://agupubs.onlinelibrary.wiley.com/doi/pdf/10.1029/2019EA000658.

Trossman, D., and Coauthors, 2020: Tracer and observationally-derived constraints on horizontal and diapycnal diffusivities in ocean models. URL http://www.essoar.org/doi/10.1002/essoar.10502123.4, archive Location: world Publisher: Earth and Space Science Open Archive Section: Oceanography, https://doi.org/10.1002/essoar.10502123.4.

Tulloch, R., and Coauthors, 2014: Direct Estimate of Lateral Eddy Diffusivity Upstream of Drake Passage. *Journal of Physical Oceanography*, **44 (10)**, 2593–2616, https://doi.org/10.1175/JPO-D-13-0120.1, URL https://journals.ametsoc.org/view/journals/phoc/44/10/jpo-d-13-0120.1.xml, publisher: American Meteorological Society Section: Journal of Physical Oceanography.

Visbeck, M., M. Dengler, T. S. Tanhua, and M. Freund, 2020: Mixing and Upwelling Dynamics along the Continental Slope off Peru inferred from Tracer Release, Hydrographic and Microstructure Measurements. AGU, URL https://agu.confex.com/agu/osm20/meetingapp.cgi/Paper/651229.

Walin, G., 1982: On the relation between sea-surface heat flow and thermal circulation in the ocean. *Tellus*, **34 (2)**, 187–195, https://doi.org/10.3402/tellusa.v34i2.10801, URL https://doi.org/10.3402/tellusa.v34i2.10801.

Waterhouse, A. F., and Coauthors, 2014: Global Patterns of Diapycnal Mixing from Measurements of the Turbulent Dissipation Rate. *Journal of Physical Oceanography*, **44 (7)**, 1854–

1872, https://doi.org/10.1175/JPO-D-13-0104.1, URL http://journals.ametsoc.org/doi/abs/10.1175/JPO-D-13-0104.1, iSBN: 0022-3670.

Waterman, S., A. C. N. Garabato, and K. L. Polzin, 2013: Internal Waves and Turbulence in the Antarctic Circumpolar Current. *Journal of Physical Oceanography*, **43 (2)**, 259–282, https://doi.org/10.1175/JPO-D-11-0194.1, URL https://journals.ametsoc.org/view/journals/phoc/43/2/jpo-d-11-0194.1.xml, publisher: American Meteorological Society Section: Journal of Physical Oceanography.

Watson, A. J., J. R. Ledwell, M.-J. Messias, B. A. King, N. Mackay, M. P. Meredith, B. Mills, and A. C. Naveira Garabato, 2013: Rapid cross-density ocean mixing at mid-depths in the Drake Passage measured by tracer release. *Nature*, **501 (7467)**, 408–411, https://doi.org/10.1038/nature12432, URL http://www.nature.com/articles/nature12432, publisher: Nature Publishing Group.

Watson, A. J., J. R. Ledwell, D. J. Webb, and C. Wunsch, 1988: Purposefully Released Tracers [and Discussion]. *Philosophical Transactions of the Royal Society of London. Series A, Mathematical and Physical Sciences*, **325 (1583)**, 189–200, URL https://www.jstor.org/stable/38109, publisher: The Royal Society.

Wenegrat, J. O., J. Callies, and L. N. Thomas, 2018: Submesoscale Baroclinic Instability in the Bottom Boundary Layer. *Journal of Physical Oceanography*, JPO–D–17–0264.1, https://doi.org/10.1175/JPO-D-17-0264.1, URL http://journals.ametsoc.org/doi/10.1175/JPO-D-17-0264.1.

Whalen, C. B., 2021: Best Practices for Comparing Ocean Turbulence Measurements across Spatiotemporal Scales. *Journal of Atmospheric and Oceanic Technology*, **38 (4)**, 837–841, https://doi.org/10.1175/JTECH-D-20-0175.1, URL https://journals.ametsoc.org/view/journals/atot/38/4/JTECH-D-20-0175.1.xml, publisher: American Meteorological Society Section: Journal of Atmospheric and Oceanic Technology.

Whalen, C. B., C. de Lavergne, A. C. Naveira Garabato, J. M. Klymak, J. A. MacKinnon, and K. L. Sheen, 2020: Internal wave-driven mixing: governing processes and consequences for climate. *Nature Reviews Earth & Environment*, **1 (11)**, 606–621, https://doi.org/10.1038/s43017-020-0097-z, URL https://www.nature.com/articles/s43017-020-0097-z, number: 11 Publisher: Nature Publishing Group.